Tracing Harmonic Distortion and Voltage Unbalance in Secondary Radial Distribution Networks with Photovoltaic Uncertainties by an Iterative Multiphase Harmonic Load Flow

J.C. Hernandez[a]* , F. J. Ruiz-Rodriguez[b] , F. Jurado[c] F. Sanchez-Sutil[a],

[b] Department of Electrical Engineering, University of Jaén, EPS Jaen, 23071, Jaén, Spain
[a] Department of Electrical and Thermal Engineering, University of Huelva, ETS de Ingeniería, 21007, Huelva, Spain
[c] Dept. of Electrical Engineering, University of Jaén, EPS Linares 23700, Jaén, Spain

Abstract

Secondary radial distribution networks (SRDNs) have been increasingly affected by the uncertainties of harmonic sources associated with photovoltaic (PV) systems. The quantitative assessment of uncertainty propagation causing harmonic distortion and voltage unbalance can be successively handled by probabilistic or affine formulations of harmonic load flows (HLFs). This study developed a general analytical technique (GAT) for solving iterative multiphase HLFs in SRDNs with PV uncertainties. This technique merges the point-estimate method (PEM) and complex affine arithmetic (AA), combined with Legendre series approximation (LGSA). It also models the input correlation. One advantage of this GAT is that the iterative harmonic penetration (IHP) method, modelled for HLF, accounts for the interaction of background harmonic voltage with the PV harmonic current. The first prerequisite was evidently an uncertainty model for PV harmonic current. This paper presents the results for a real unbalanced three-phase SRDN and compares them with those obtained with the Monte-Carlo simulation (MCS). These confirmed the accuracy of GAT as well as its lower computational cost. The numerical results obtained showed that the GAT outperformed the incomplete GAT (IGAT), which is solely based on PEM and Cornish-Fisher expansion, thanks to the ability of AA to bound the outputs used in the LGSA.

Keywords: Harmonic load flow; Point estimate methods; Complex affine arithmetic; PV system; Harmonic distortion; Unbalance.

Nomenclature

A	area
$B\text{-}1$	number of SRDN nodes with traditional generator
C	constraint at fundamental-frequency
$C\text{-}B$	number of SRDN nodes with LDs
D	data
G	global irradiance
h	harmonic
$H_g\,(H_d)$	global (diffuse) irradiation
i	any given SRDN node
$\vec{J}$	current in branch
m	moment
n_{rv}	number of random input variables
n_{su}	number of sources of uncertainty
N	number of SRDN nodes
n_{LG}	number of terms in LGSA
n_x	number of points considered in x-axis of a CDF
$N\text{-}C+1$	number of SRDN nodes with PV systems
p	real (active) power
q	reactive power
$R\,(X)$	resistance (reactance)
$\vec{S}$	apparent power
t	t-th 10-min time interval
THD	total harmonic distortion
TPD	total phase distortion
TPU	total phase unbalance
u, v, z	uncertain variable
$\vec{V}\,(\vec{I})$	fundamental and harmonic voltage (current) phasors
x	random variable
$\vec{Y}$	admittance
$\vec{Z}$	impedance
$\left[\vec{Y}_{bus}\right]$	SRDN nodal admittance matrix

* Corresponding author. Tel.: Tel.: +34 953 212463; Fax: +34 953 212478

E-mail addresses: jcasa@ujaen.es (J.C. Hernandez), javier.ruiz@die.uhu.es (F. J. Ruiz-Rodriguez), fjurado@ujaen.es (F. Jurado), F. Sanchez-Sutil (fssutil@ujaen.es).

α significance level
β non-standardised coefficient
γ electrical efficiency
$[\imath]$ identity matrix
$\vec{\Gamma}$ network parameter phasor
δ standard location
ε symbolic variables that lies in the interval [-1,1]
ζ state variable
θ phase angle
κ cumulant
$\lambda^3(\lambda^4)$ skewness (kurtosis)
$\mu(\sigma)$ expected value (standard deviation)
$(\Upsilon^{(2)})\Upsilon^{(0)}$ ratio of the (negative)zero sequence to the positive sequence
$\vec{\Xi}$ network input phasor
ξ average-root-mean-square error
$\vec{\Pi}$ network state variable phasor
τ tilted surface
ς tolerance error
ϕ^{-1} inverse of the univariate standard normal distribution
Φ any constant
$\psi = \sum_{i=1}^{n} |u_i| - u_{err}$
$\vec{\Psi}$ network output phasor
ω weighting factor
$(\varpi_j = \varpi_{vth-wth\ pu})$ ϖ_j-th fundamental-frequency normalized current interval
[ ] interval form of a uncertain variable/ or matrix notation
$\mathbb{P}$ probability
$\mathbb{R}$ set of real number
$f^{'}$ PDF of random variable
f PDF of random variable
F CDF of random variable
F^{-1} inverse distribution function of the random variable

Superscripts

c any given point on a CDF
d, j, s any given number
GAT general analytical technique
h any given fundamental- or harmonic frequency $(h = 1,2,,...,h_{\max})$
I current
(k) (d) general iteration numbers
(p) any given phase in a SRDN node (*p= a, b, c*)
r order of moment or cumulant
(s) any given sequence in a SRDN node (*s=0, 1, 2*)
V voltage
θ phase angle
% relative magnitude
-spec typical spectrum
$\hat{}$ affine form of a uncertain variable
* complex conjugate
$\oplus$ to refer a real (active) current
$\odot$ normalized value
$\bar{}$ upper bound or supremum
$\breve{}$ to refer a given location
$\frown$ to refer to primitive impedance matrix for four-wire grounded wye lines

Subscripts

a to refer the real coefficient (partial deviation) of the uncertain variable
bus nodal
d diffuse
err error
g global
h any given harmonic frequency
i, j any given node of the SRDN (i= 1,2,…,*N*)
$i_{(LD)}$ any given LD node of SRDN $(i_{(LD)} = B, B+1, ..., C\text{-}1)$
$i_{(pv)}$ any given PV system node of the SRDN $(i_{(pv)} = C, C+1, ..., N)$
I current
L branch
m any given number
max maximum
K *K*th location
M modified
n_{su} number of sources of uncertainty
o to refer the central value of the uncertain variable
pv photovoltaic
R reduced
t *t*-th 10-min time interval
v (w) *v*th(*w*th) fundamental-frequency normalized current level
V voltage
x random variable *x*
$\underline{}$ lower bound or infimum
ϖ_j ϖ_j-th fundamental-frequency normalized current interval
τ tilted surface

Abbreviations

AA affine arithmetic
CDF cumulative distribution function
CLF conventional load flow
CLFm modified CLF
GAT general analytical technique
HLF harmonic load flow
HP harmonic penetration
IA interval arithmetic
IHA iterative harmonic analysis
IHP iterative harmonic penetration
LD linear device (load/generator)
LGSA Legendre series approximation
LV low voltage
MCS Monte-Carlo simulation
NLD non-linear device
PDF probability density function
PEM point-estimate method
PV photovoltaic
SRDN secondary radial distribution network
VN voltage node method

1. Introduction

Because of their relatively low power, PV systems are generally connected to SRDNs. The coupling of PV systems to such networks often leads to technical problems, such as loss increase [1], errors in control signals and measuring [2-4], harmonic distortion [5-11], resonance events [12-14] and voltage unbalance [15,16]. The analysis of problems generated by PV harmonics in SRDNs and their resolution has thus become an increasingly important concern for utilities. Harmonic problems within an unbalanced network are also an issue of growing interest [17- 22].

Mathematical methods for analyzing harmonics in power systems usually have a deterministic basis, namely, a deterministic HLF [23]. Such methods can be direct [17-20,24-31] or iterative/integrated [21,22,32- 37]. Iterative

methods take into account the interaction of background harmonic voltage with the harmonic current of non-linear devices (NLDs). Although their assessment is more accurate, their computational burden grows as the problem becomes more complex.

Balanced HLFs have been widely addressed in literature [18,24,25,28-37] since the normal operation of transmission and distribution systems assumes the voltage to be symmetric. However, more accurate models have been designed for unbalanced three-phase conditions [15-20], which can even account for the previously mentioned interactions [21,22].

Grid-connected PV power sources are unpredictable because of cloud transients and seasonal effects [38,39]. Therefore, their exploitation brings multiple correlated PV uncertainties [40] into the SRDN, which stem from the geographically closer location. Other traditional uncertainties come from time variations of phase-load demands and network configuration [41,42]. This makes it necessary to deal with the HLF analysis by using probabilistic or affine formulations, which analyze the system states, based on all input probable values or the bounds of the probable values, respectively.

In the technical literature, there are various methodologies that can be used to deal with the impact of the PV input uncertainties in power systems. It is true that the MCS is widely employed [43-45] but its computational cost is still very high [46], despite improvements such as Latin Hypercube sampling [47,48]. In order to reduce the computational effort, the following set of methods was applied: (i) analytical methods (e.g. the fast Fourier transform method [49] or the cumulants method combined with series expansion [38,39,50-53]); (ii) approximate methods, (e.g. the first-order second-moment method [54], the method based on AA [55], and the PEM [40,56]; (iii) fuzzy logic methods [57]). There are no holistic criteria for evaluating different methods, and compromise is often made between computational speed and accuracy. Nonetheless, the second group of methods was sufficient to provide planners and designers with the results needed to make objective decisions [58].

Currently, the probabilistic approaches for evaluating harmonic distortion and voltage unbalance with PV systems are of great interest [7,9-11,15,16] because standards usually specify the 95%-probability level as the power quality index. For example, the EN 50160 [59] and IEC 61000-2-2 standards [60] mention this percentile in reference to the limit of the compatibility level. This means that knowledge of the whole output distribution is needed for standards application [61]. As harmonic distortion and voltage unbalance can have various adverse effects, the control and limitation of harmonic current emission from new PV systems is essential for maintaining supply voltage distortions below the prescribed compatibility or planning levels. This is also required to ensure electromagnetic compatibility.

As reflected in the literature on HLFs with uncertainties, analyses are generally performed using direct methods. Accordingly, the study in [27] focused on the impact of the random nature of magnitude and phase angle for harmonic inputs. References [24,25] compared two methods for modelling harmonic sources in large real MV distribution networks using aggregate harmonic source models parameterized based on measurements for different customer categories. Reference [25] applied a method for analyzing HLFs based on possibility theory. This research not only dealt with correlated inputs for LDs and NLDs, but also informed about the output distributions. Other studies [17,18,29,31] used analytical methods, mainly the PEM [62], to analyze uncertainty propagation throughout the system. Various improvements were proposed in [28] to overcome the deficiencies of the PEM, such as solely focusing on the harmonic voltage magnitude. Regarding the approximation expansions for probability density functions (PDFs), [18,30] developed two methodologies with MCS data to approximate the distribution functions THD_V and harmonic voltage (magnitude and phase angle). The research in [19] used complex AA [63] to solve a three-phase HLF and thus provide

the infimum and supremum in a correlated approach to uncertain variables. Following this HLF analysis for unbalanced three-phase conditions, [20] analyzed uncertainty propagation with MCS but limited the inputs to a set of previously defined clusters.

In regard to iterative methods, HLFs were mainly performed on a deterministic basis [21,22,32,33]. Approaches with uncertainties have almost always implemented the MCS, as reflected in the analysis of a multiconverter power system in [34,35,37]. Nonetheless, approximate methods have rarely taken an iterative approach [36].

References [3,15,16,64-66] focused on capturing PV harmonic behavior with deterministic direct HLFs, whereas [67-69] opted for probabilistic direct approaches. In particular, references [15,16] analyzed the impact of a single-phase PV system location on the negative-sequence voltage in a stochastic way, considering background unbalance. The dynamic interaction of different PV plants connected to the same bus was analyzed in [66] to validate the practical constraints in assessing grid-code compliance requirements. However, to the best of our knowledge, there have been no iterative analyses performed for PV systems.

This general review of literature on HLFs with uncertainties [17-37], complemented with that on PV systems [3,15,16,64-69], clearly indicates that the assessment of HLF in the PV context is an issue that has not as yet been studied in sufficient depth. The biggest problem is that no analytical methods, (or approximate methods except for [36]) have been applied to the solution of iterative HLFs with uncertainties. MCS is generally used for such cases [34,35,37], but when iterative methods are involved, the resulting computational burden is huge. As a result, direct probabilistic-formulation HLFs are a frequent research focus [17,18,20,24-31]. Moreover, in those rare cases when the correlation between inputs is included [18,25,30], only the fundamental-frequency is involved. Nor is there any information regarding behavior models of NLD harmonic current versus background harmonic voltage for phase angles (except in [30]). To make matters worse, output phase-angle uncertainties are rarely assessed (except in [24,25,30]). To date, probabilistic- and affine-formulation HFLs have mainly analyzed meshed test systems [18,28-30,34-37] as compared to radial configurations [19,20,25,31] and have focused on NLDs at only a few nodes, with the exception of [16].

In order to overcome some of these limitations, this study developed a GAT for solving iterative multiphase HLFs in SRDNs with PV uncertainties. This new technique uses the PEM [70] and complex AA [63,71] combined with LGSA. As shown in [72], LGSA is able to estimate bounded random variables more accurately than other approximations. The PEM determines the moments of output variables, whose upper and lower bounds are calculated with an AA-based method. Then both results are used for LGSA.

Our GAT is thus an innovative tool that extends deterministic iterative multiphase HLF to the stochastic field. It is able to analyze SRDNs with multiple PV and load demand uncertainties, given the following:

- The IHP method accounts for background harmonic interaction.
- It has the ability to handle correlated variables.
- It provides an accurate model of PV harmonic current behavior versus background harmonic voltage [72].
- By using PEM and complex AA, the same routines as those of a deterministic iterative approach can be used. This gives accurate results with a low computational burden.
- The LGSA is better able to reconstruct bounded output variables than other approximations [72].
- The whole PDF of output variables is determined and used for checking the regulatory limit fulfilment.
- The aggregated effect of several PV systems distributed throughout SRDNs can be analyzed.

In addition, the GAT merges a probabilistic HLF formulation, based on the PEM, and an interval HLF formulation, based on complex AA. This substantially enhances the level of accuracy obtained with only one of the formulations without a substantial increase in computational cost

The paper is organized as follows. Section 2 outlines the power quality indices used throughout the paper. Section 3 introduces AA, and Section 4 describes system uncertainty modelling. Section 5 explains the deterministic HLF, whereas Section 6 focuses on the probabilistic one. Section 7 presents and discusses the results obtained for a real SRDN in Spain. Finally, Section 8 summarizes the conclusions that can be derived from this research.

2. Extended indices for harmonic distortion and unbalance

Existing power-quality standards [59,60] consider the following indices for harmonic distortion e.g. for voltage: total harmonic distortion of voltage in phase *p* ($THD_{V^{(p)}}$) [73]. Voltage unbalance can be characterized by a different unbalance factor [40]. Generally addressed is the ratios of the negative- and zero-sequence voltage to the positive-sequence voltage at the *h*th-order harmonic [74] (($\Upsilon_V^{(2)h}$, $\Upsilon_V^{(0)h}$). This can be generalized to three-phase systems that are subject to the waveform unbalance and distortion resulting from the coupling effect between sequences at each harmonic order. For this purpose, the symmetrical component linear transformation of Fortescue [75] was applied in [76], namely $[\vec{V}^{(p)h}] \Rightarrow [\vec{V}^{(s)h}]$. This transformation permitted the formulation of more refined indices, capable of characterizing and maintaining a consistent distinction between the individual effects of harmonic distortion and unbalance. Consequently, the index of the total phase distortion of voltage, TPD_V is preferable to the conventional $THD_{V^{(p)}}$ index [76]:

$$TPD_V = \frac{\sqrt{\sum_{h=2}^{\infty}\left[\left(V^{(0)h}\right)^2+\left(V^{(1)h}\right)^2+\left(V^{(2)h}\right)^2\right]}}{\sqrt{\left(V^{(0)1}\right)^2+\left(V^{(1)1}\right)^2+\left(V^{(2)1}\right)^2}} \tag{1}$$

The new unbalance index, namely, the total phase unbalance of voltage is [76]:

$$TPU_V = \frac{\sqrt{\sum_{h=1}^{\infty}\left[\left(V^{(0)3h-1}\right)^2+\left(V_0^{(0)3h-2}\right)^2+\left(V^{(1)3h-1}\right)^2+\left(V^{(1)3h-3}\right)^2+\left(V^{(2)3h-2}\right)^2+\left(V^{(2)3h-3}\right)^2\right]}}{\sqrt{\sum_{h=1}^{\infty}\left[\left(V^{(0)3h-3}\right)^2+\left(V^{(1)3h-2}\right)^2+\left(V^{(2)3h-1}\right)^2\right]}} \tag{2}$$

And the fundamental phase unbalance of voltage TPU_{V^1} can be obtained with the addition in (2) limited to *h*=1.

3. Interval and affine arithmetic

AA [71] is a general term for numerical methods that are used to produce intervals for bounding all possible outputs, when dealing with sources of uncertainty. AA is analogous to interval arithmetic (IA), but it can describe uncertainty in a simpler form and effectively deals with the interdependencies of parameters. Hence, IA solution conservativeness can be mitigated as compared to IA [71].

An uncertain variable, *u* can be expressed as a linear polynomial in real AA, namely, its real affine form $\hat{u}$:

$$\hat{u} = u_o + \sum_{a=1}^{n_{su}} u_a \varepsilon_a + u_{err}\varepsilon_{err_u} \tag{3}$$

Each ε_a represents one of n_{su} sources of uncertainty. The final term $u_{err}\varepsilon_{err_u}$ is an approximation error term.

Let *u, v* be two uncertain variables, the fundamental mathematical operations in real AA are introduced as follows [63]:

$$\hat{z} = \hat{u} \pm \hat{v} = (u_o \pm v_o) + \sum_{a=1}^{n_{su}} (u_a \pm v_a)\varepsilon_a + (u_{err} \pm v_{err})\varepsilon_{err_z}$$

$$\hat{z} = \Phi \hat{u} = \Phi u_o + \Phi \sum_{a=1}^{n_{su}} u_a \varepsilon_a + \Phi u_{err} \varepsilon_{err_z} \tag{4}$$

$$\hat{z} = \hat{u} \pm \Phi = (u_o \pm \Phi) + \sum_{a=1}^{n_{su}} u_a \varepsilon_a + u_{err} \varepsilon_{err_z}$$

$$\hat{z} = \hat{u} \cdot \hat{v} = u_o \cdot v_o + \sum_{a=1}^{n_{su}} (u_o v_a + v_o u_a)\varepsilon_a + u_o v_{err} \varepsilon_{err_v} + v_o u_{err} \varepsilon_{err_u} + \sum_{a=1}^{n_{su}} \left(u_a \varepsilon_a + u_{err} \varepsilon_{err_u}\right) \cdot \sum_{a=1}^{n_{su}} \left(v_a \varepsilon_a + v_{err} \varepsilon_{err_v}\right) \tag{5}$$

Let f be a general function with n_{su} uncertain input variables $(\hat{u}_1, \hat{u}_2, ..., \hat{u}_{n_{su}})$ the output is then determined in (6). In this expression, z_{n+1} is an extra error approximation term, which is necessary as not all operations on affine forms result in an affine combination of ε_a:

$$\hat{z} = f(\hat{u}_1, \hat{u}_2, ..., \hat{u}_{n_{su}}) = f(u_{o_1} + u_{1_1}\varepsilon_1,\ u_{o_2} + u_{1_2}\varepsilon_2,\ ...,\ u_{o_{n_{su}}} + u_{1_{n_{su}}}\varepsilon_{n_{su}}) = z_o + z_1\varepsilon_1 + z_2\varepsilon_2 + ..., + z_{n_{su}}\varepsilon_{n_{su}} + z_{n_{su}+1}\varepsilon_{n_{su}+1} \tag{6}$$

When f is a non-affine operation, $\hat{z}$ cannot be represented precisely as an affine combination of the noise symbols ε_a. However, an affine approximation function can be assumed with different structures, depending on the desired degree of accuracy and the available computational resources [71].

Let $\vec{u}$ and $\vec{v}$ be two complex numbers, the real AA can be transferred to the complex space with complex AA. Consequently, common operations follow the same rules as real AA [77], and the multiplication is expressed in (7). A more in-depth analysis of complex AA operators is given in [63]:

$$\hat{\vec{z}} = \hat{\vec{u}} \cdot \hat{\vec{v}} = u_o \cdot v_o + \sum_{a=1}^{2n_{su}} (u_o v_a + v_o u_a)\varepsilon_a + \left[\sum_{a=1}^{2n_{su}} g(u_a)\right] \cdot \left[\sum_{a=1}^{2n_{su}} g(v_a)\right] \varepsilon_{2n_{su}+1}$$
$$\text{with } g(\vec{z}) = |xx| + j|yy| \quad \text{if } \vec{z} = xx + jyy \tag{7}$$

When *a* is odd, u_a and v_a are real coefficients; and when *a* is even, u_a and v_a are imaginary coefficients.

The affine and interval forms of an uncertain variable can be converted from one to the other. Given a variable u in interval form, $[u] = [\underline{u}, \overline{u}] := \{u \in \mathbb{R} \mid \underline{u} \le u \le \overline{u}\}$, the corresponding affine form $\hat{u}$ can be expressed as (8). Each affine form in (3) can be converted to an interval form by (9). It should be stated that conversion from affine to interval forms results in the loss of all information regarding the correlation of parameters. Moreover, the boundary results computed by the IA are often much larger than those of the AA.

$$\hat{u} = u_o + u_1\varepsilon_1 = \frac{\underline{u} + \overline{u}}{2} + \frac{\overline{u} - \underline{u}}{2}\varepsilon_1 \tag{8}$$

$$[\underline{u}, \overline{u}] = [u_o - \psi, u_o + \psi], \quad \text{with} \quad \psi = \sum_{a=1}^{n_{su}} |u_a| - u_{err} \tag{9}$$

4. Uncertainty modelling for the SRDN

This section describes uncertainty modelling for the SRDN, as applied to linear devices (LDs) and PV systems. Both probabilistic and affine models are included. Distribution lines and cables are generally modelled for HLF analysis as deterministic lumped parameter elements [78].

4.1. Load modelling

4.1.1. Modelling of fundamental-frequency load

The probabilistic and affine modelling of the fundamental-frequency load in this research is directly based on smart meter measurements over a period of several years, i.e. historical data [40]. This made it possible to stochastically characterize by moments (probabilistic model) and lower/upper bounds (affine model) a typical load profile of the real and reactive power $\left(\left[p^{(\mathrm{p})1}_{i_{(\mathrm{LD})},t} \right], \left[q^{(\mathrm{p})1}_{i_{(\mathrm{LD})},t} \right]\right)$ for each t-th 10-min time interval, $i_{(\mathrm{LD})}$th SRDN node, and phase p during time period of one year.

4.1.2. Modelling of harmonic load

The most commonly used models of harmonic load for HLF analysis are parallel connections [23,79,80]. Generally speaking, the models can be written as:

$$\left[\vec{Y}^{(\mathrm{p})h}_{i_{(\mathrm{LD})},t} \right] = g^{h}_{i_{(\mathrm{LD})}} \left(\left[\vec{Y}^{(\mathrm{p})1}_{i_{(\mathrm{LD})},t} \right], h \right) \qquad (i_{(\mathrm{LD})} = B, B+1, \ldots, C\text{-}1;\ h=3,5,\ldots,H) \tag{10}$$

4.2. PV modelling

The probabilistic and affine modelling of PV systems was developed by the authors in [72] and designed as a current source [24] at fundamental and harmonic frequency. The background harmonic interaction was also modelled.

4.2.1. Modelling for PV fundamental-frequency current

The PV modelling is based on [38,39], and is specified for 10-min intervals. Accordingly, the meteorological random/uncertain variables involved are the global and diffuse irradiation on the horizontal plane $(H_{g;\, i_{(\mathrm{pv})},t}, H_{d;\, i_{(\mathrm{pv})},t})$ for a certain $i_{(\mathrm{pv})}$th PV location (SRDN node) and t-th 10-min interval. Both random/uncertain irradiations determine the τ-tilt global irradiance, $G_{\tau;\, i_{(\mathrm{pv})},t}$. Subsequently, the per-unit PV fundamental-frequency power is given as:

$$p^{1}_{i_{(\mathrm{pv})},t} = \gamma_{i_{(\mathrm{pv}),\,t}} \cdot A \cdot G_{\tau;\, i_{(\mathrm{pv})},t} \tag{11}$$

Its affine form shows the sources of uncertainty for the affine model:

$$\hat{p}^{1}_{i_{(\mathrm{pv})},t} = f(\hat{H}_{g;\, i_{(\mathrm{pv})},t}, \hat{H}_{d;\, i_{(\mathrm{pv})},t}) = f(\varepsilon_{H_{g;\, i_{(\mathrm{pv})},t}}, \varepsilon_{H_{d;\, i_{(\mathrm{pv})},t}}, \varepsilon_{err_{p^{1}_{i_{(\mathrm{pv})},t}}}) \tag{12}$$

The cumulant method [81] and complex AA [71] in (11) and (12), respectively, determine the cumulants (probabilistic model) and upper/lower bounds (affine model) for the random/uncertain variable, $p^{1}_{i_{(\mathrm{pv})},t}$ from those of $H_{g;i_{(\mathrm{pv})},t}$ and $H_{d;\, i_{(\mathrm{pv})},t}$. Next, the random or uncertain variable, real per-unit PV fundamental-frequency current in phase p $(\left|\vec{I}^{(\mathrm{p})1,\oplus}_{i_{(\mathrm{pv})},t}\right|$ or $\left|\hat{\vec{I}}^{(\mathrm{p})1,\oplus}_{i_{(\mathrm{pv})},t}\right|)$ is computed from the PV inverter efficiency and a 1-p.u. AC fundamental-frequency phase voltage. Finally, an approximation expansion [82,83] gives its PDF.

4.2.2. Modelling for PV harmonic current

The stochastic harmonic model based on measurements are widely used in literature [24,25,84]. Therefore, the statistical PV harmonic current in [72] is computed with a method composed of two phases (Fig. 1). The first phase deals with the statistical characterization of the typical PV harmonic current spectrum (relative magnitude and phase angle) at different fundamental-frequency current intervals, based on [85]. The second phase provides the distribution functions of the PV harmonic current (absolute magnitude[2] and phase angle) on the basis of the harmonic spectrum statistical characterization and the PV fundamental-frequency current.

[2] Unless otherwise specified magnitude refers to absolute magnitude

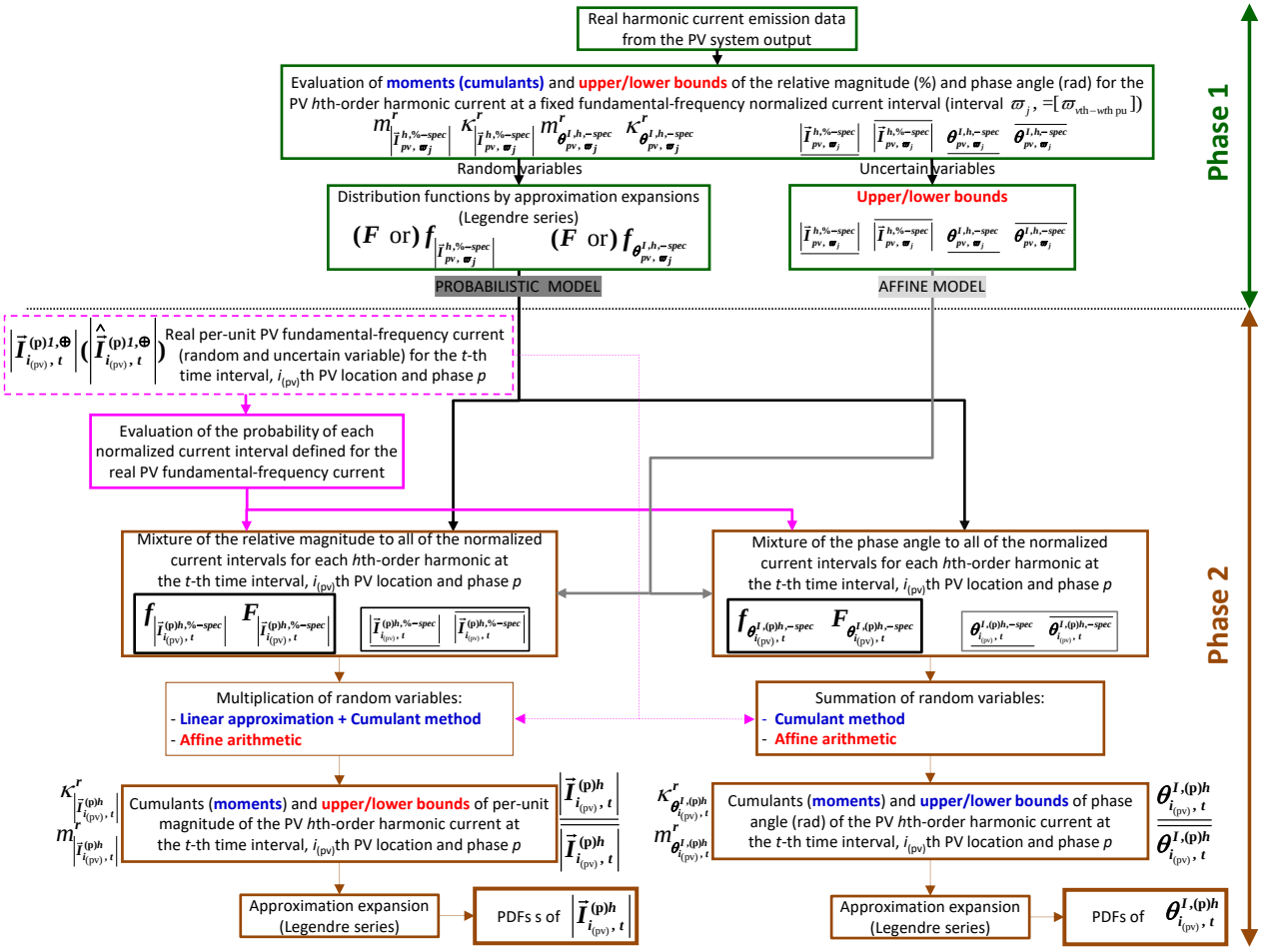

Fig. 1. *Flowchart of the probabilistic and affine model for the PV harmonic current.*

In the second phase, the probabilistic mode determines the PV harmonic current for a point of interest (i.e., for a *t*-th time interval, $i_{(pv)}$th PV location, and phase *p*) from two random variables specified for that point of interest, namely, the typical PV *h*th-order harmonic current spectrum and the above-mentioned PV fundamental-frequency current, $I_{i_{(pv)},t}^{(p)1,\oplus}$. To model the first one, the probability of each ϖ_j-th interval for the point of interest is evaluated. Next, by using these probability weights, a mixture distribution is applied to the typical PV *h*th-order harmonic current spectrum (relative magnitude $\left|\vec{I}_{pv,\,\varpi_j}^{\,h,\%-spec}\right|$ and phase angle $\theta_{pv,\,\varpi_j}^{I,h,-spec}$) for all of the ϖ_j-th intervals. This provides the PDF and cumulative distribution functions (CDF) of the PV *h*th-order harmonic current spectrum specified for the point of interest $\left(\left|\vec{I}_{i_{(pv)},t}^{(p)h,\%-spec}\right|, \theta_{i_{(pv)},t}^{I,(p)h,-spec}\right)$. The *h*th-order harmonic current (per-unit absolute magnitude and phase angle) is then given for the point of interest by [80]:

$$\left|\vec{I}_{i_{(pv)},t}^{(p)h}\right| = \left|\vec{I}_{i_{(pv)},t}^{(p)1,\oplus}\right| \cdot \left|\vec{I}_{i_{(pv)},t}^{(p)h,\%-spec}\right| \qquad (i_{(pv)} = C, C+1, \ldots, N;\quad h=3,5,\ldots,H;\quad p=a,b,c) \tag{13}$$

$$\theta_{i_{(pv)},t}^{(p)I,h} = \theta_{i_{(pv)},t}^{(p)I,h,-spec} + h\cdot\left(\theta_{i_{(pv)},t}^{(p)I,1} - \theta_{i_{(pv)},t}^{(p)I,1,-spec}\right) \qquad (i_{(pv)} = C, C+1, \ldots, N;\quad h=3,5,\ldots,H;\quad p=a,b,c) \tag{14}$$

In the case of the affine model, a mixture procedure is solved by AA as well. This provides the affine form of the PV *h*th-order harmonic current spectrum specified for the point of interest. Accordingly, the *h*th-order harmonic current is [80]:

$$\left|\hat{\vec{I}}_{i_{(pv)},t}^{(p)h}\right| = \left|\hat{\vec{I}}_{i_{(pv)},t}^{(p)1,\oplus}\right| \cdot \left|\hat{\vec{I}}_{i_{(pv)},t}^{h,\%-spec}\right| \qquad (i_{(pv)} = C, C+1, \ldots, N;\quad h=3,5,\ldots,H;\quad p=a,b,c) \tag{15}$$

$$\hat{\theta}_{i_{(pv)},t}^{(p)I,h} = \hat{\theta}_{i_{(pv)},t}^{(p)I,h,-spec} + h\cdot\left(\hat{\theta}_{i_{(pv)},t}^{(p)I,1} - \hat{\theta}_{i_{(pv)},t}^{(p)I,1,-spec}\right) \qquad (i_{(pv)} = C, C+1, \ldots, N;\quad h=3,5,\ldots,H;\quad p=a,b,c) \tag{16}$$

To statistically characterize the random output variables in the probabilistic mode, a linear approximation [52] is firstly applied to the multiplication of random variables in (13). The cumulant method [81] is subsequently applied to (13) and (14). This allows for the cumulant evaluation [86,87] of random outputs. In the affine model, (15) and (16) are

solved with complex AA by providing the upper and lower bounds of uncertain output variables. Finally, the LGSA reconstructs the resulting variables in terms of PDFs.

4.2.3. Modelling of background harmonic voltage interaction on PV harmonic current

A multiple linear regression model was developed by the author in [85] to assess the interaction of the background *j*th-order harmonic voltage on the typical PV *h*th-order harmonic current spectrum at different ϖ_j-th intervals:

$$\begin{aligned}\Delta\left|\vec{I}_{pv,\,\varpi_j}^{\,h,-spec}\right| &= \beta_{\varpi_j,\,h}^{\mathrm{I},\,j,-spec}\cdot\left|\vec{V}^{\,j}\right| \\ \Delta\theta_{pv,\,\varpi_j}^{I,h,-spec} &= \beta_{\varpi_j,\,h}^{\theta,\,j,-spec}\cdot\left|\vec{V}^{\,j}\right|\end{aligned} \tag{17}$$

Based on this model, this section describes the interaction model for a point of interest, namely, for a *t*-th time interval, phase *p*, and $i_{(\mathrm{pv})}$th PV location. The probability of each ϖ_j-th interval is evaluated for the point of interest by (18). The resulting coefficient for the point of interest is then computed by using these probability weights on each interval coefficient (19) for all of the ϖ_j-th intervals.

$$\mathbb{P}_{i_{(\mathrm{pv})},\,t,\,\varpi_j} = \mathbb{P}(v\text{th pu} \le \overset{\ominus}{I}{}_{i_{(\mathrm{pv})},\,t}^{(\mathrm{p})1,\oplus} \le w\text{th pu}) = F_{\overset{\ominus}{I}{}_{i_{(\mathrm{pv})},\,t}^{(\mathrm{p})1,\oplus}}(w\text{th pu}) - F_{\overset{\ominus}{I}{}_{i_{(\mathrm{pv})},\,t}^{(\mathrm{p})1,\oplus}}(v\text{th pu}) \tag{18}$$

$$\beta_{i_{(\mathrm{pv})},\,t,\,h}^{j} = \sum_{\varpi_j}\mathbb{P}_{i_{(\mathrm{pv})},\,t,\,\varpi_j}\cdot\beta_{\varpi_j,\,h}^{j,-spec} \tag{19}$$

The linear model for the background harmonic interaction is:

$$\begin{aligned}\Delta\left|\vec{I}_{i_{(\mathrm{pv})},\,t}^{\,(\mathrm{p})h}\right| &= \beta_{i_{(\mathrm{pv})},\,t,\,h}^{\mathrm{I},\,(\mathrm{p})j}\cdot\left|\vec{V}_{i_{(\mathrm{pv})},\,t}^{\,(\mathrm{p})j}\right| \qquad (i_{(\mathrm{pv})} = C, C{+}1, \ldots, N;\;\; h{=}3,5,\ldots,H;\;\; p = a,b,c) \\ \Delta\theta_{i_{(\mathrm{pv})},\,t}^{I,(\mathrm{p})h} &= \beta_{i_{(\mathrm{pv})},\,t,\,h}^{\theta,\,(\mathrm{p})j}\cdot\left|\vec{V}_{i_{(\mathrm{pv})},\,t}^{\,(\mathrm{p})j}\right|\end{aligned} \tag{20}$$

5. Deterministic HLF

HLFs can be stated in a power-flow non-linear equation form [30,88]. Since this formulation results in convergence problems for SRDNs, the admittance matrix formulation for SRDNs is the standard practice [79]. In this regard, the simplest numerical method for solving deterministic HLFs is harmonic penetration (HP), which assumes no harmonic interaction between the network and NLDs [17-20,24,28-31]. Nevertheless, the recognized IHP accounts for the interaction of the harmonic voltage with NLD behavior [21,32,34,35-37].

The IHP method in Fig. 2 consists of three steps: (i) fundamental-frequency conventional load flow (CLF) modified (CLFm); (ii) iterative harmonic analysis (IHA); and (iii) voltage node method (VN). Sinusoidal voltage is assumed in the NLD-1 block whereas harmonic voltage is assumed in the NLD-2 block. The method can be summarized as follows:

<u>Step 1:</u> Modified CLF (CLFm)

Substep 1-1: The CLFm is computed by taking into account the LD node constraints (21), which are also applied to PV system nodes with PV system behavior. Accordingly, the fundamental-frequency voltages $\left[\vec{V}_{i,\,t}^{\,(\mathrm{p})1}\right]$ are:

$$G_i\left(\left[\vec{V}_{i,\,t}^{\,(\mathrm{p})1}\right],\left[\vec{I}_{i,\,t}^{\,(\mathrm{p})1}\right]\right) = \left[c_{i,\,t}^{(\mathrm{p})}\right]; \qquad (i = 1,2,\ldots,N) \tag{21}$$

The most commonly used methodologies for computing CLF have problems with convergence [89] for multiphase formulations in SDRNs. Consequently, this research used the method in [90].

The fundamental-frequency LD admittance for each phase *p* and $\mathrm{i}_{(\mathrm{LD})}$*th* SRDN node can be computed from the CLFm solution:

$$\left[\vec{Y}^{(\mathbf{p})1}_{i_{(\mathrm{LD}),t}}\right]=\begin{bmatrix}\vec{Y}^{(\mathbf{a})1}_{i_{(\mathrm{LD}),t}}\\ \vec{Y}^{(\mathbf{b})1}_{i_{(\mathrm{LD}),t}}\\ \vec{Y}^{(\mathbf{c})1}_{i_{(\mathrm{LD}),t}}\end{bmatrix}=\begin{bmatrix}\left(\vec{S}^{(\mathbf{a})1*}_{i_{(\mathrm{LD}),t}}\right)^{*}\Big/\left|\vec{V}^{(\mathbf{a})1}_{i_{(\mathrm{LD}),t}}\right|^{2}\\ \left(\vec{S}^{(\mathbf{b})1*}_{i_{(\mathrm{LD}),t}}\right)^{*}\Big/\left|\vec{V}^{(\mathbf{b})1}_{i_{(\mathrm{LD}),t}}\right|^{2}\\ \left(\vec{S}^{(\mathbf{c})1*}_{i_{(\mathrm{LD}),t}}\right)^{*}\Big/\left|\vec{V}^{(\mathbf{c})1}_{i_{(\mathrm{LD}),t}}\right|^{2}\end{bmatrix} \qquad (i_{(\mathrm{LD})}=B,B+1,\ldots,C\text{-}1;\ p=a,b,c) \tag{22}$$

The harmonic LD admittances are given as:

$$\left[\vec{Y}^{(\mathrm{p})h}_{i_{(\mathrm{LD}),t}}\right]=g^{h}_{i_{(\mathrm{LD})}}\left(\left[\vec{Y}^{(\mathrm{p})1}_{i_{(\mathrm{LD}),t}}\right],h\right) \qquad (i_{(\mathrm{LD})}=B,B+1,\ldots,C\text{-}1;\ p=a,b,c;\ h=3,5,\ldots,h_{\max}) \tag{23}$$

The admittances of generators and LD loads are included in the SRDN nodal admittance matrix in harmonic domain $\left[\vec{Y}^{(\mathrm{p})h}_{bus,t}\right]$, which is given by (24), (see Fig. 4) thus forming the modified SRDN admittance matrix $\left[\vec{Y}^{(\mathrm{p})h}_{busM,t}\right]$. The SRDN is then reduced to the PV system nodes to obtain the reduced matrix $\left[\vec{Y}^{(\mathrm{p})h}_{busR,t}\right]$.

$$\left[\vec{Y}^{(p)h}_{bus,t}\right]=\begin{bmatrix}\frac{1}{\left[\vec{Z}^{(\mathrm{p}),\mathrm{h}}_{\text{Root node}}\right]}+\sum_{\mathrm{m}}\frac{1}{\left[\vec{Z}^{(\mathrm{p}),\mathrm{h}}_{\mathrm{L}_{1\mathrm{m}}}\right]}+\sum_{\mathrm{m}}\frac{\left[\vec{Y}^{(\mathrm{p}),\mathrm{h}}_{\mathrm{L}_{1\mathrm{m}}}\right]}{2} & \cdots & \cdots & \cdots\\ \cdots & \cdots & \cdots & \cdots\\ \cdots & \sum_{\mathrm{m}}\frac{1}{\left[\vec{Z}^{(\mathrm{p}),\mathrm{h}}_{\mathrm{L}_{\mathrm{im}}}\right]}+\sum_{\mathrm{m}}\frac{\left[\vec{Y}^{(\mathrm{p}),\mathrm{h}}_{\mathrm{L}_{\mathrm{im}}}\right]}{2} & \cdots & -\frac{1}{\left[\vec{Z}^{(\mathrm{p}),\mathrm{h}}_{\mathrm{L}_{\mathrm{iN}}}\right]}\\ \cdots & \cdots & \cdots & \sum_{\mathrm{m}}\frac{1}{\left[\vec{Z}^{(\mathrm{p}),\mathrm{h}}_{\mathrm{L}_{\mathrm{mN}}}\right]}+\sum_{\mathrm{m}}\frac{\left[\vec{Y}^{(\mathrm{p}),\mathrm{h}}_{\mathrm{L}_{\mathrm{mN}}}\right]}{2}\end{bmatrix} \tag{24}$$

<u>Step 2:</u> IHA

Substep 2-1: the values at the *k*th iteration of the harmonic voltages $\left[\vec{V}^{(\mathrm{p})h,(k)}_{i_{(\mathrm{pv}),t}}\right]$ update more accurate PV harmonic currents by means of (20). This can be written as:

$$\left[\vec{I}^{(\mathrm{p})h,(k)}_{i_{(\mathrm{pv}),t}}\right]=H^{(\mathrm{p})h}_{i_{(\mathrm{pv}),t}}\left(\left[\vec{V}^{(\mathrm{p})1}_{i_{(\mathrm{pv}),t}}\right],\left[\left|\vec{V}^{(\mathrm{p})h,(k)}_{i_{(\mathrm{pv}),t}}\right|\right],\left[\zeta^{(\mathrm{p})s,(k)}_{i_{(\mathrm{pv}),t}}\right],\left[D^{(\mathrm{p})d}_{i_{(\mathrm{pv}),t}}\right]\right);\ (i_{(\mathrm{pv})}=C,\ldots,N;s=1,\ldots,s_{\max};d=1,\ldots,d_{\max};h=3,\ldots,h_{\max}) \tag{25}$$

Substep 2-2: the convergence of PV harmonic current results $\left[\vec{I}^{(\mathrm{p})h,(k)}_{i_{(\mathrm{pv}),t}}\right]$ is verified. Otherwise, it is necessary to proceed to the next substep.

Substep 2-3: the harmonic currents are then applied to update new harmonics voltages:

$$\left[\vec{V}^{(\mathrm{p})h}_{i_{(\mathrm{pv}),t}}\right]^{(k+1)}=\left[\vec{Y}^{(\mathrm{p})h}_{busR,t}\right]^{-1}\left[\vec{I}^{(\mathrm{p})h}_{i_{(\mathrm{pv}),t}}\right]^{(k)}; \qquad (i_{(\mathrm{pv})}=C,C+1,\ldots,N;\ h=3,5,\ldots,h_{\max}) \tag{26}$$

The process is then redirected back to substep 2-1.

<u>Step 3:</u> VN

Substep 3-1: the VN determines the nodal harmonic voltages by incorporating PV injected currents to the nodal current:

$$\left[\vec{V}^{(\mathrm{p})h}_{bus,t}\right]=\left[\vec{Y}^{(\mathrm{p})h}_{busM,t}\right]^{-1}\left[\vec{I}^{(\mathrm{p})h,(k)}_{bus,t}\right]; \qquad (h=3,5,\ldots,h_{\max}) \tag{27}$$

The symmetrical component transformation [75] then determines the harmonic voltages in the symmetrical component-based framework:

$$\left[\vec{V}^{(\mathrm{s})h}_{bus,t}\right]=[T]\left[\vec{V}^{(\mathrm{p})h}_{bus,t}\right]; \qquad (h=3,5,\ldots,h_{\max}) \tag{28}$$

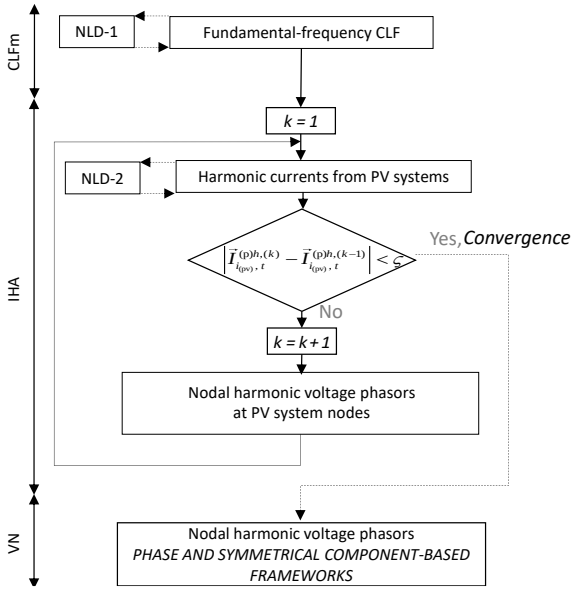

Fig. 2. *Flowchart of the numerical solution method for the deterministic HLF by IHP.*

6. Probabilistic and affine HLF

A good way to characterize the sources of uncertainty in HLFs is to model inputs as uncertain or random variables. In this regard, the MCS and our GAT are simulation techniques that make it possible to keep using the deterministic HLF routine.

6.1. MCS for solving probabilistic HLFs

MCS is a statistical simulation method that randomly selects values of input variable distributions, and with these values, solves various deterministic HLFs in Section 5. The probabilistic solution of the output variables is reconstructed from computed deterministic data. The computational burden required by applying MCS to the HLF is enormous because of the dimensions of the equation system and the number of trials required to obtain a satisfactory level of accuracy. It is well known that high precision can always be achieved with this method, which is why it is often used as a reference method that others can be compared to.

6.2. Proposed GAT for the HLF

Fig. 3 shows the GAT developed in this research. This innovative technique is capable of calculating the harmonic voltage distributions (magnitude and phase angle) at each $i_{(LD)}$*th* SRDN node and phase *p* in two stages. The first stage uses the PEM to determine the first statistical moments of the harmonic voltages, and applies the AA-based method to compute the bounds. Both formulations are based on the statistical characterization of the input variables. The second stage uses LGSA to estimate the output distributions from the bounds and moments of the variables. However, for purposes of comparison, we also designed the IGAT, which estimates output distributions, based only on the moment by the Cornish-Fisher approximation. The affine-HLF computation burden is thus unnecessary.

6.2.1. PEM-based methodology for solving HLFs

The formulation of a deterministic HLF constitutes an equation system written as:

$$\vec{\Xi} = G(\vec{\Pi}, \vec{\Gamma}); \quad \vec{\Psi} = H(\vec{\Pi}, \vec{\Gamma}) \tag{29}$$

A particular *i*th solution of $\vec{\Psi}$ is given by $\vec{\Psi}_i = F(\vec{\Pi})$.

The uncertainties of random inputs of PV systems $\vec{I}_{i_{(pv)}}$ and LDs $\vec{S}^1_{i_{(LD)}}$ in the HLF can be satisfactorily assessed with a probabilistic approach (i.e., the PEM). The PEM concentrates the statistical information of the first few moments of a random input variable $x_{j,t}$ at *K* deterministic locations $\bar{x}_{j,K,t}$. Given function F, which connects input and output

variables, as well as previous locations, the statistical moments of random outputs can be computed. This research considered $2\,n_{rv}+1$ schemes [70]. The procedure consisted of the following steps:

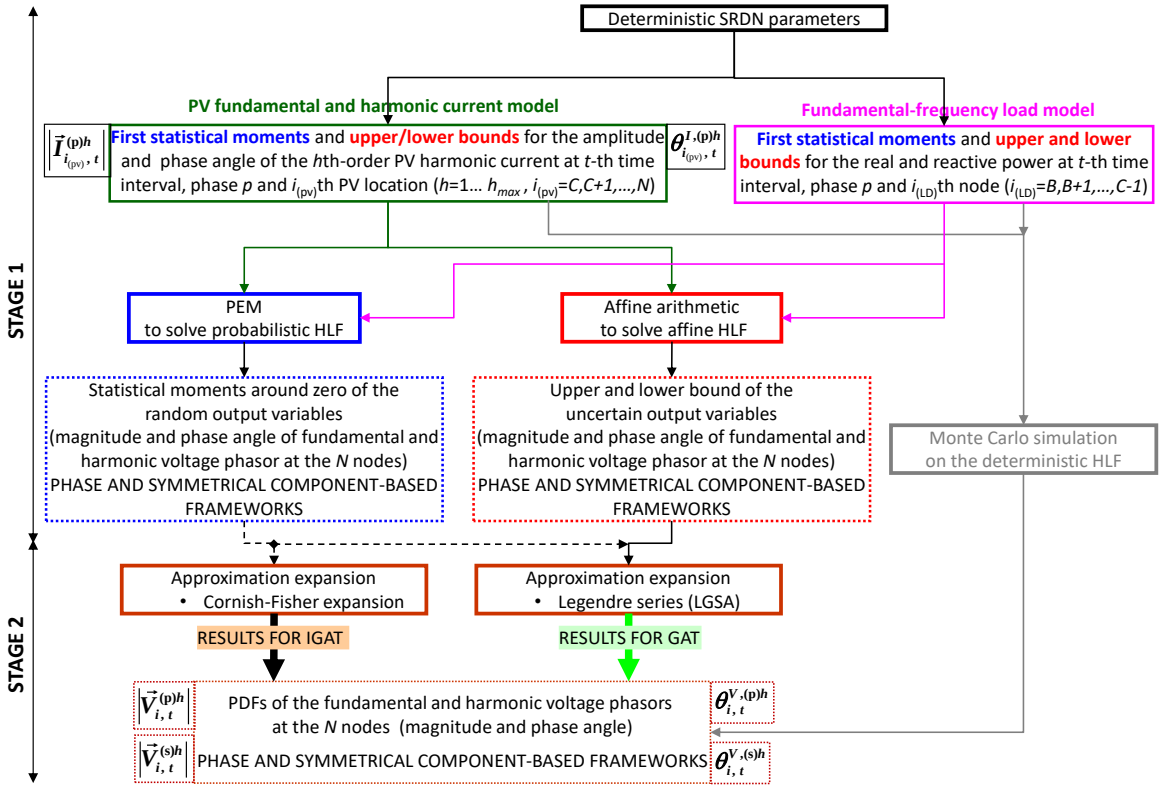

Fig. 3. *Flowchart of the proposed GAT.*

- The rotational transformation method in [40,52] transforms the set of n_{rv} correlated random inputs $(p^{(p)1}_{i_{(LD)},t}, q^{(p)1}_{i_{(LD)},t}, \left|\vec{I}^{(p)h}_{i_{(pv)},t}\right|, \theta^{I,(p)h}_{i_{(pv)},t})$, into a set of n_{rv} uncorrelated random inputs $(x_{1,t}, x_{2,t}, ..., x_{j,t}, ..., x_{n_{rv},t})$. This is necessary in the presence of input correlation. PV powers of geographically closer locations are correlated [40,41]. There are also reasons for the correlation between nodal loads [40,41].

- The so-called Kth concentration $(\breve{x}_{x_{j,t},K},\ \omega_{x_{j,t},K})$ of each random input $x_{j,t}$ is obtained from the statistical input data (e.g. PDF, i.e., $f_{x_{j,t}}$):

$$\breve{x}_{x_{j,t},K} = \mu_{x_{j,t}} + \delta_{x_{j,t},K} \cdot \sigma_{x_{j,t}}; \qquad (K = 1,2) \tag{30}$$

The two standard locations and weights are [70]:

$$\delta_{x_{j,t},K} = \lambda^3_{x_{j,t}}/2 + (-1)^{3-K} \cdot \sqrt{\lambda^4_{x_{j,t}} - 3/4 \cdot \left(\lambda^3_{x_{j,t}}\right)^2}; \quad \omega_{x_{j,t},K} = (-1)^{3-K} / [\delta_{x_{j,t},K} \cdot (\delta_{x_{j,t},1} - \delta_{x_{j,t},2})]; \quad (K = 1,2) \tag{31}$$

- The function F is evaluated only two times for each random input $x_{j,t}$ at the points specified for the Kth location $\breve{x}_{x_{j,t},K}$ of the random input $x_{j,t}$ and the expected value of the n_{rv} -1 remaining inputs, namely $(\mu_{x_{1,t}}, \mu_{x_{2,t}}, ..., \mu_{\breve{x}_{j,K,t}}, ..., \mu_{x_{n_{rv},t}})$.

- One additional evaluation of function F at the point specified for the n_{rv} expected value of random inputs $(\mu_{x_{1,t}}, \mu_{x_{2,t}}, ..., \mu_{x_{j,t}}, ..., \mu_{x_{n_{rv},t}})$ is required with the following specific weighting factor:

$$\omega_{o,t} = 1 - \sum_{j=1}^{n_{rv}} \left[1/(\lambda^4_{x_{j,t}} - \left(\lambda^3_{x_{j,t}}\right)^2 \right] \tag{32}$$

- The solution for each of the preceding deterministic HLF is:

$$\vec{\Psi}_i\left(x_{j,t},K\right)=F(\mu_{x_{1,t}},\mu_{x_{2,t}},...,\mu_{\hat{x}_{x_{j,t},K}},...,\mu_{x_{n_{rv},t}}) \tag{33}$$

- The vector $\vec{\Psi}_i\left(x_{j,t},K\right)$ is used to estimate the *r*th-order statistical moments around zero of the random output variables $\vec{\Psi}_i$ (*i.e.*, $\left|\vec{V}_{1,t}^{(\mathrm{p/s})h}\right|,\theta_{1,t}^{V,(\mathrm{p/s})h},\left|\vec{V}_{2,t}^{(\mathrm{p/s})h}\right|,\theta_{2,t}^{V,(\mathrm{p/s})h},...,\left|\vec{V}_{N,t}^{(\mathrm{p/s})h}\right|,\theta_{N,t}^{V,(\mathrm{p/s})h}$):

$$E\left(\vec{\Psi}_i^r\right)\cong\sum_{j=1}^{n_{rv}}\sum_{K=1}^{2}\omega_{x_{j,t},K}\cdot\left[\vec{\Psi}_i\left(x_{j,t},K\right)\right]^r+\omega_{o,t}\cdot\left[F(...,\mu_{x_j},...)\right]^r \tag{34}$$

6.2.2. AA-based methodology for solving HLFs

The affine HLF is an advanced development of the deterministic HLF described in section 5. It consists of the following steps.

<u>Step 1:</u> Affine CLFm

Substep 1-1: The fundamental-frequency CLF is solved in complex AA [55,91,92] by the method in [90], which accounts for the behavior of PV systems. This method consists of the iterative forward and backward sweep process (see Fig. 4a).

1. Initialization: all voltage magnitudes are assumed to be 1 p.u. and their phase angles 0º, 120º, and -120° phase shifted. The set of uncertain input variables that represents the real per-unit PV fundamental-frequency currents and LD power injections are expressed in complex affine form ($\left[\hat{\vec{I}}_{i_{(\mathrm{pv})},t}^{(\mathrm{p})1,\oplus}\right],\left[\hat{\vec{S}}_{i_{(\mathrm{LD})},t}^{(\mathrm{p})1}\right]$), involving n_{su} noise symbols.
2. Forward sweep: at iteration *d*, the uncertain current at the extreme LD node of the SRDN, i.e., node #*j*, is:

$$\left[\hat{\vec{I}}_{j,t}^{(\mathrm{p})1,(d)}\right]=\begin{bmatrix}\hat{\vec{I}}_{j,t}^{(\mathrm{a})1,(d)}\\ \hat{\vec{I}}_{j,t}^{(\mathrm{b})1,(d)}\\ \hat{\vec{I}}_{j,t}^{(\mathrm{c})1,(d)}\end{bmatrix}=\begin{bmatrix}\left(\hat{\vec{S}}_{j_{(\mathrm{LD})},t}^{(\mathrm{a})1}\right)^*\Big/\hat{\vec{V}}_{j,t}^{(\mathrm{a})1,(d-1)}\\ \left(\hat{\vec{S}}_{j_{(\mathrm{LD})},t}^{(\mathrm{b})1}\right)^*\Big/\hat{\vec{V}}_{j,t}^{(\mathrm{b})1,(d-1)}\\ \left(\hat{\vec{S}}_{j_{(\mathrm{LD})},t}^{(\mathrm{c})1}\right)^*\Big/\hat{\vec{V}}_{j,t}^{(\mathrm{c})1,(d-1)}\end{bmatrix} \tag{35}$$

The uncertain voltage at node #*i* and branch current L_{ij} can be determined from the current at node #*j*, as follows:

$$\begin{aligned}&\left[\hat{\vec{V}}_{i,t}^{(\mathrm{p})1,(d)}\right]=\left[\vec{a}_{L_{ij}}^{(\mathrm{p}),1}\right]\left[\hat{\vec{V}}_{j,t}^{(\mathrm{p})1,(d)}\right]-\left[\vec{b}_{L_{ij}}^{(\mathrm{p}),1}\right]\left[\hat{\vec{I}}_{j,t}^{(\mathrm{p})1,(d)}\right];\\ &\left[\hat{\vec{I}}_{L_{ij},t}^{(\mathrm{p})1,(d)}\right]=-\left[\vec{c}_{L_{ij}}^{(\mathrm{p}),1}\right]\left[\hat{\vec{V}}_{j,t}^{(\mathrm{p})1,(d)}\right]+\left[\vec{d}_{L_{ij}}^{(\mathrm{p}),1}\right]\left[\hat{\vec{I}}_{j,t}^{(\mathrm{p})1,(d)}\right]\end{aligned} \tag{36}$$

where the matrices are stated in [90]. According to Fig. 4b:

$$\begin{aligned}&\left[\vec{a}_{L_{ij}}^{(\mathrm{p}),1}\right]=\left[\vec{d}_{L_{ij}}^{(\mathrm{p}),1}\right]=\left[\iota^{(\mathrm{p})}\right]+\frac{1}{2}\left[\vec{Z}_{L_{ij}}^{(\mathrm{p}),1}\right]\left[\vec{Y}_{L_{ij}}^{(\mathrm{p}),1}\right];\\ &\left[\vec{b}_{L_{ij}}^{(\mathrm{p}),1}\right]=\left[\vec{Z}_{L_{ij}}^{(\mathrm{p}),1}\right];\\ &\left[\vec{c}_{L_{ij}}^{(\mathrm{p}),1}\right]=\left[\vec{Y}_{L_{ij}}^{(\mathrm{p}),1}\right]+\frac{1}{4}\left[\vec{Y}_{L_{ij}}^{(\mathrm{p}),1}\right]\left[\vec{Z}_{L_{ij}}^{(\mathrm{p}),1}\right]\left[\vec{Y}_{L_{ij}}^{(\mathrm{p}),1}\right];\end{aligned} \tag{37}$$

Taking into account both the uncertain LD current at node #*i*, obtained by (35) and the PV current, the uncertain total current at node #*i* is:

$$\left[\hat{\vec{I}}_{i,t}^{(\mathrm{p})1,(d)}\right]=\left[\hat{\vec{I}}_{i_{(\mathrm{LD})},t}^{(\mathrm{p})1,(d)}\right]+\left[\hat{\vec{I}}_{L_{ij},t}^{(\mathrm{p})1,(d)}\right]-\left[\hat{\vec{I}}_{i_{(\mathrm{pv})},t}^{(\mathrm{p})1,\oplus}\right] \tag{38}$$

Voltages and currents per phase at root node #*1*, are obtained by (36).

3. Convergence judgment: when the convergence criterion is verified, the following result is obtained:

$$\max\left(\left|\underline{\hat{V}^{(\mathrm{p})1}_{\text{Root node},\,t}}-\underline{\hat{V}^{(\mathrm{p})1,(d)}_{1,\,t}}\right|,\left|\overline{\hat{V}^{(\mathrm{p})1}_{\text{Root node},\,t}}-\overline{\hat{V}^{(\mathrm{p})1,(d)}_{1,\,t}}\right|\right)\le\varsigma;\quad (p=a,b,c) \tag{39}$$

4. Backward sweep: the reference voltage $\left[\vec{V}^{(\mathrm{p})1,}_{\text{Root node},\,t}\right]$ is considered at node #*1*. The uncertain voltages at the successive nodes are calculated with the currents in step 2. For example, the voltage of node #*i* is:

$$\left[\hat{\vec{V}}^{(\mathrm{p})1,(d)}_{i,\,t}\right]=\left[\vec{a}^{(\mathrm{p}),1}_{L_{1i}}\right]^{-1}\left[\vec{V}^{(\mathrm{p})1,}_{\text{Root node},\,t}\right]-\left[\vec{a}^{(\mathrm{p}),1}_{L_{1i}}\right]^{-1}\left[\vec{b}^{(\mathrm{p}),1}_{L_{1i}}\right]\left[\hat{\vec{I}}^{(\mathrm{p})1,(d)}_{i,\,t}\right] \tag{40}$$

With the preceding voltages, the iterative process begins again at the second step.

Once convergence is achieved, the fundamental-frequency LD admittances are:

$$\vec{Y}^{(\mathrm{p})1}_{i_{(\mathrm{LD})},\,t}=\frac{\vec{S}^{(\mathrm{p})1*}_{i_{(\mathrm{LD})},\,t,o}}{\left|\vec{V}^{(\mathrm{p})1}_{i_{(\mathrm{LD})},\,t,o}\right|^2};\ \text{e.g. }\vec{Y}^{(\mathrm{a})1}_{i_{(\mathrm{LD})},\,t}=\frac{\vec{S}^{(\mathrm{a})1*}_{i_{(\mathrm{LD})},\,t,o}}{\left|\vec{V}^{(\mathrm{a})1}_{i_{(\mathrm{LD})},\,t,o}\right|^2};\ (i_{(\mathrm{LD})}=B,B{+}1,\ldots,C{-}1;\ p=a,b,c) \tag{41}$$

The harmonic LD admittances are given by:

$$\left[\vec{Y}^{(\mathrm{p})h}_{i_{(\mathrm{LD})},\,t}\right]=g^{h}_{i_{(\mathrm{LD})}}\left(\left[\vec{Y}^{(\mathrm{p})1}_{i_{(\mathrm{LD})},\,t}\right],h\right);\qquad (i_{(\mathrm{LD})}=B,B{+}1,\ldots,C{-}1;\ h{=}3,5,\ldots,h_{\max}) \tag{42}$$

The harmonic LD admittances are incorporated into SRDN admittance matrix $\left[\vec{Y}^{(\mathrm{p})h}_{bus,\,t}\right]$, building modified SRDN admittance matrix $\left[\vec{Y}^{(\mathrm{p})h}_{busM,\,t}\right]$. In addition, the system is reduced to the PV system nodes, which obtains reduced matrix $\left[\vec{Y}^{(\mathrm{p})h}_{busR,\,t}\right]$.

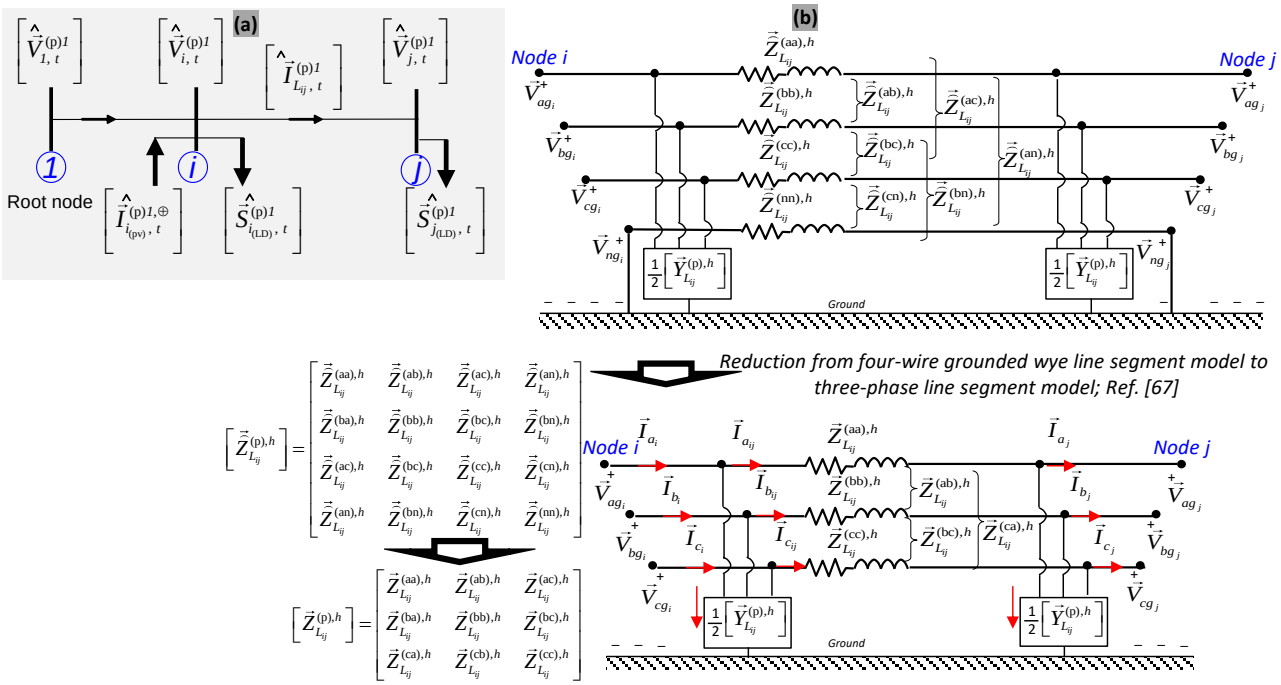

Fig. 4. *Example of an SRDN with 3 nodes (a) and its three-phase line segment model (b).*

<u>Step 2:</u> Affine IHA

Substep 2-1: the uncertain harmonic voltages $\left[\hat{\vec{V}}^{(\mathrm{p})h,(k)}_{i_{(\mathrm{pv})}}\right]$ at the *k*th iteration are used to update more accurate PV harmonic currents by solving (20). By using a Cartesian-to-Polar transformation for voltages and a Polar-to-Cartesian transformation for current, (20) can be written as:

$$\left[\hat{\vec{I}}^{(\mathrm{p})h,(k)}_{i_{(\mathrm{pv})},\,t}\right]=H^{(\mathrm{p})h}_{i_{(\mathrm{pv})},\,t}\left(\hat{\vec{V}}^{(\mathrm{p})1}_{i_{(\mathrm{pv})},\,t},\left|\vec{V}^{(\mathrm{p})h,(k)}_{i_{(\mathrm{pv})},\,t,\,o}\right|,\zeta^{(\mathrm{p})s,(k)}_{i_{(\mathrm{pv})},\,t},D^{(\mathrm{p})d}_{i_{(\mathrm{pv})},\,t}\right);\ (i_{(\mathrm{pv})}=C,\ldots,N;\ s=1,\ldots,s_{\max};\ d=1,\ldots,d_{\max};\ h=3,\ldots,h_{\max}) \tag{43}$$

Substep 2-2: the convergence criterion is verified for PV harmonic current results, thus transforming them into interval forms such as (39). Otherwise, it is necessary to proceed to the next step.

Substep 2-3: the harmonic currents then derive the new iteration for uncertain harmonic voltages:

$$\left[\hat{\vec{V}}_{i_{(\mathrm{pv})},\,t}^{(\mathrm{p})h}\right]^{(k+1)} = \left[\vec{Y}_{busR,\,t}^{(\mathrm{p})h}\right]^{-1}\left[\hat{\vec{I}}_{i_{(\mathrm{pv})},\,t}^{(\mathrm{p})h}\right]^{(k)}; \qquad (i_{(\mathrm{pv})} = C, C+1, \ldots, N;\ h = 3,5,\ldots,h_{\max}) \tag{44}$$

The process is then redirected back to Substep 2-1.

<u>Step 3:</u> Affine VN

Substep 3-1: the VN determines the uncertain nodal harmonic voltages by incorporating PV-injected currents into the nodal current vector:

$$\left[\hat{\vec{V}}_{bus,\,t}^{(\mathrm{p})h}\right] = \left[\vec{Y}_{busM,\,t}^{(\mathrm{p})h}\right]^{-1}\left[\hat{\vec{I}}_{bus,\,t}^{(\mathrm{p})h,(k)}\right]; \qquad (h = 3,5,\ldots,h_{\max}) \tag{45}$$

The symmetrical component transformation [75] then determines the uncertain harmonic voltages in the symmetrical component-based framework:

$$\left[\hat{\vec{V}}_{bus,\,t}^{(\mathrm{s})h}\right] = [T]\left[\hat{\vec{V}}_{bus,\,t}^{(\mathrm{p})h}\right]; \qquad (h = 3,5,\ldots,h_{\max}) \tag{46}$$

6.2.3. Output distribution by approximation expansion

As reflected in the literature, any PDF of a random variable x with finite cumulants can be expressed in terms of orthogonal polynomial expansions [81]. The most widely used expressions are the Gram-Charlier type A and Laguerre polynomial expansion [83]. Among the Saddle Point approximations are the Edgeworth [83] and Cornish-Fisher [82] expansions. Previous series are defined for an interval $-\infty \le x \le +\infty$. For this reason, they do not consider that x can only take values within an interval $\underline{x} \le x \le \overline{x}$. For an optimal performance, knowledge of the upper and lower bounds is also necessary. This is accomplished by using the LGSA [72,93], which is for a finite interval $0 \le t \le 1$. The form of the LGSA can handle many moments, and even more important, it uses direct knowledge of the upper and lower bounds. Since the Gram-Charlier and Edgeworth expansions employ orthogonal polynomials based on a normal distribution, their applicability is limited to nearly normal distributions [30]. Since this study analyzes strongly asymmetric distributions, only Cornish-Fisher expansions and LGSA were applied.

7. Case studies

The software code was MATLAB using a computer with Intel® Core™ i7-8750H+HM370 (6 cores), 2.2-4.1 GHz, and 16-GB DDR4. A rural SRDN was used as a case study for this work. Unless otherwise stated, the results focused on node #30, the most critical multiphase node for voltage regulation.

The GAT analyzed harmonic distortion and voltage unbalance in two scenarios. The first scenario (#1) was a 10-min time interval around 12:00 p.m. (midday) for a cloudy winter day in January. The second scenario (#2) was 10-min interval at the same time for a sunny summer day July.

7.1.1. Test SRDN data and PV input data

The SRDN was a 30-branch, 31-node, 0.4-kV SRDN located in a rural area of Andalusia [40]. It was a four-wire SRDN with a multigrounded neutral system. It should be highlighted that this rural SRDN had unbalanced lines and line sections, carrying a mixture of single-phase, double-phase, and three-phase loads. The base allocation and sizing of PV

systems in [40] for each node and phase is shown in Fig. 5. This amounted to 15 PV systems of 10 kWp, which meant a 10%-PV penetration.

The first statistical moments and bounds for global and diffuse irradiation, based on specific geolocation (node), were obtained from [40], which provided PV correlation data as well. Statistical data (moments and bounds) and correlation for each real/reactive fundamental-frequency node load and phase were derived from [40]. PV harmonic data were gathered by time-domain measurements [85], which involved both the typical PV harmonic current spectrum and the background harmonic interaction.

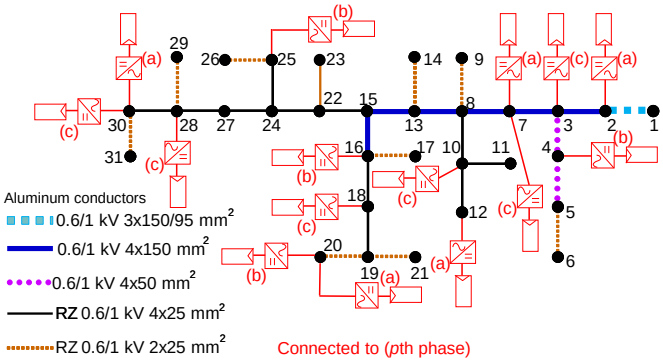

***Fig. 5**. Single-line diagram of the rural SRDN.*

7.1.2. PV harmonic current injection

This section presents the PDFs, resulting from the procedure outlined in section 4.2.2. They are for the PV harmonic current in each scenario, and focus on the 10-kWp PV system at node #30 and phase *a*. Magnitude results are given in p.u., and the power and line-to-neutral voltage base were chosen as 1-MVA and 230-V, respectively.

As a common behavior pattern for lower-order harmonic currents (3rd-order, 5th-order, and 7th-order harmonics) in January vs. July lower absolute magnitude levels in the PDFs were observed mainly because of the lower levels of fundamental-frequency current, even though the relative magnitude levels in the relevant PDFs were greater. However, the magnitude levels for higher-order harmonics hardly changed in the two months. Regarding the phase angles, levels moved somewhat erratically from higher to lower values when compared both months.

Any known distribution could be identified in the PDFs thus obtained. In January, the PDF shape was farthest away from a Gaussian distribution. This outcome agrees with [72] since the harmonic current PDF begins to show a more Gaussian behavior as the fundamental-frequency current level increases.

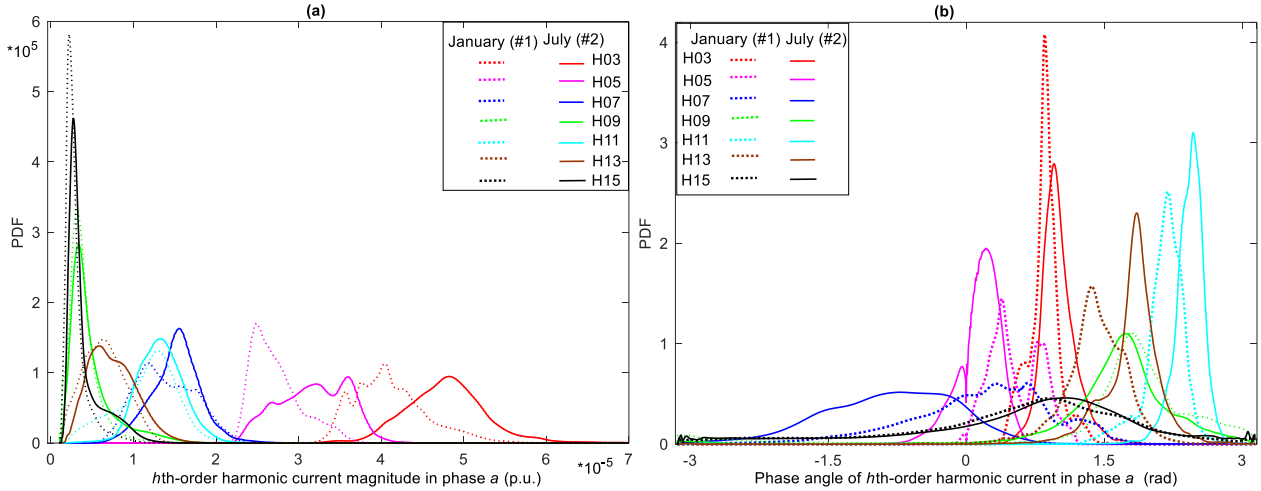

***Fig. 6.** PDF curves of the hth-order harmonic current for the PV system at node #30 and phase a, on a day of January/July at 12:00 p.m. (midday): (a) magnitude; (b) phase angle.*

7.1.3. Accuracy and computation cost of the GAT versus MCS

To demonstrate the accuracy of the GAT, its results in the test SRDN with PV systems were compared with those of the MCS for 10,000 trials, which was used as a reference. This assessment was carried out, based on an average-root-mean-square error index of the resulting CDFs. In particular, this error in the harmonic voltage magnitude, $\left|\vec{V}_{i,t}^{(\mathrm{p})h}\right|$ (phase angle, $\theta_{i,t}^{V,(\mathrm{p})h}$) is given by [39]:

$$\xi^{\mathrm{GAT}}_{\left|\vec{V}_{i,t}^{(\mathrm{p})h}\right|(\theta_{i,t}^{V,(\mathrm{p})h})} = \frac{\sqrt{\sum_{c=1}^{n_x}\left(F^{\mathrm{GAT},\,c}_{\left|\vec{V}_{i,t}^{(\mathrm{p})h}\right|(\theta_{i,t}^{V,(\mathrm{p})h})} - F^{\mathrm{MCS},\,c}_{\left|\vec{V}_{i,t}^{(\mathrm{p})h}\right|(\theta_{i,t}^{V,(\mathrm{p})h})}\right)^2 / \left(F^{\mathrm{MCS},\,c}_{\left|\vec{V}_{i,t}^{(\mathrm{p})h}\right|(\theta_{i,t}^{V,(\mathrm{p})h})}\right)^2}}{n_x} \cdot 100 \tag{47}$$

and the maximum error for all of the SRDN nodes and phases:

$$\xi^{\mathrm{GAT}}_{\left|\vec{V}_{\mathrm{max},\,t}^{(\max)h}\right|(\theta_{\mathrm{max},\,t}^{V,(\max)h})} = \max_{i,p}\left\{\xi^{\mathrm{GAT}}_{\left|\vec{V}_{i,t}^{(\mathrm{p})h}\right|(\theta_{i,t}^{V,(\mathrm{p})h})}\right\} \tag{48}$$

Although the Cornish-Fisher expansion and Legendre series can be based on any number of cumulants or terms, respectively, this research used the first five cumulants [39,72] and the first five/twenty terms [72].

Table 1 shows a condensed collection of results for the maximum GAT errors of the harmonic voltages in the SRDN. As can be observed, the GAT had a high level of accuracy for all harmonics. In fact, the more terms used in the LGSA, the greater its accuracy was with very little variation in the computation time. Consequently, there was no increase in the computational burden. MCS was found to be computationally expensive, and thus not viable for the purposes of this analysis.

Regarding the results for 20 terms, when the harmonic order was higher, the error in harmonic voltage magnitude was greater. Nevertheless, the accuracy for higher harmonic orders was closely tied to lower ones. For phase-angle accuracy, there was no change. The most significant error occurred in scenario #2, July. As a result, a higher dispersion in the resulting PDF led to an increase in errors. Finally, the comparison of errors for the SRDN nodes revealed that the greatest errors occurred in PV system nodes.

Table 1. Maximum GAT error of all node harmonic voltages and associated computation time.

Time interval	Error (%)	n_{LG}	Node, Phase	Harmonic order							Computation time (s)	
				3	5	7	9	11	13	15	GAT	MCS
$t_{\#1}$ (January)	$\xi^{\mathrm{GAT}}_{\left\|\vec{V}^{(\max)h}_{\mathrm{max},\,t_{\#1}}\right\|}$	20	(#, phase *p*)	(#30, *a*)	(#30, *a*)	(#30, *a*)	(#30, *a*)	(#30, *a*)	(#30, *a*)	(#30, *a*)		
				1.85	1.24	0.89	1.72	1.92	2.12	4.46	85.06	51038.92
		5		3.98	3.50	2.95	2.94	3.43	5.49	6.18	83.36	50528.52
	$\xi^{\mathrm{GAT}}_{\theta^{V,(\max)h}_{\mathrm{max},\,t_{\#2}}}$	20	(#, phase *p*)	(#30, *a*)	(#30, *a*)	(#30, *a*)	(#30, *a*)	(#30, *a*)	(#30, *a*)	(#30, *a*)	==	==
				1.16	1.23	1.27	1.37	1.48	1.44	1.54	==	==
		5		3.80	3.59	6.55	6.76	8.66	6.34	7.18		
$t_{\#2}$ (July)	$\xi^{\mathrm{GAT}}_{\left\|\vec{V}^{(\max)h}_{\mathrm{max},\,t_{\#2}}\right\|}$	20	(#, phase *p*)	(#30, *a*)	(#30, *a*)	(#30, *a*)	(#30, *a*)	(#30, *a*)	(#30, *a*)	(#30, *a*)		
				2.06	1.37	1.44	2.05	1.65	2.81	4.81	44.23	29857.71
		5		4.11	4.12	3.91	3.78	2.75	5.84	6.87	43.35	29559.13
	$\xi^{\mathrm{GAT}}_{\theta^{V,(\max)h}_{\mathrm{max},\,t_{\#2}}}$	20	(#, phase *p*)	(#30, *a*)	(#30, *a*)	(#30, *a*)	(#30, *a*)	(#30, *a*)	(#30, *a*)	(#30, *a*)		
				1.27	1.26	1.16	1.48	1.54	1.50	1.58	==	==
		5		4.22	4.23	6.34	6.97	8.03	6.55	6.76	==	==

7.1.4. The GAT versus incomplete IGAT

This section discusses the accuracy of the GAT as compared to the IGAT. For both techniques and various harmonics, Fig. 7 displays the results of harmonic voltage magnitude in node #30 (phase *a*) with background harmonic

interaction on a July day at 12:00 p.m. (midday) Fig. 8 focuses on the voltage unbalance, whereas the rest of the variables remain the same as in the previous figure.

As can be observed, the error index ξ highlights that the fitting by the GAT was clearly more precise than that of the IGAT for all of the results. For example, Fig. 7b indicates that the GAT better reconstructed the peaks and troughs of the PDF. It also shows a curve that is much closer to the MCS for the 5th-order harmonic. Moreover, the GAT limited the PFD from the lower to the upper bounds, thanks to the LGSA. Conversely, the IGAT prolonged the PDF beyond its bounds. As expected, both techniques produced large errors in derived variables (see Fig. 8b), namely, the unbalance computed from all of the harmonic voltages.

The 7th-order harmonic showed the most non-Gaussian behavior, followed by the 15th-order, 3rd-order and 5th-order harmonics. This result agrees with the non-Gaussian shape of input variables in Fig. 6.. Nevertheless, according to central limit theorem, the PDF of output variables tended to show a more Gaussian behavior. In fact, the behavior of the output variables was quite different from the non-Gaussian behavior of the inputs in Fig. 6.

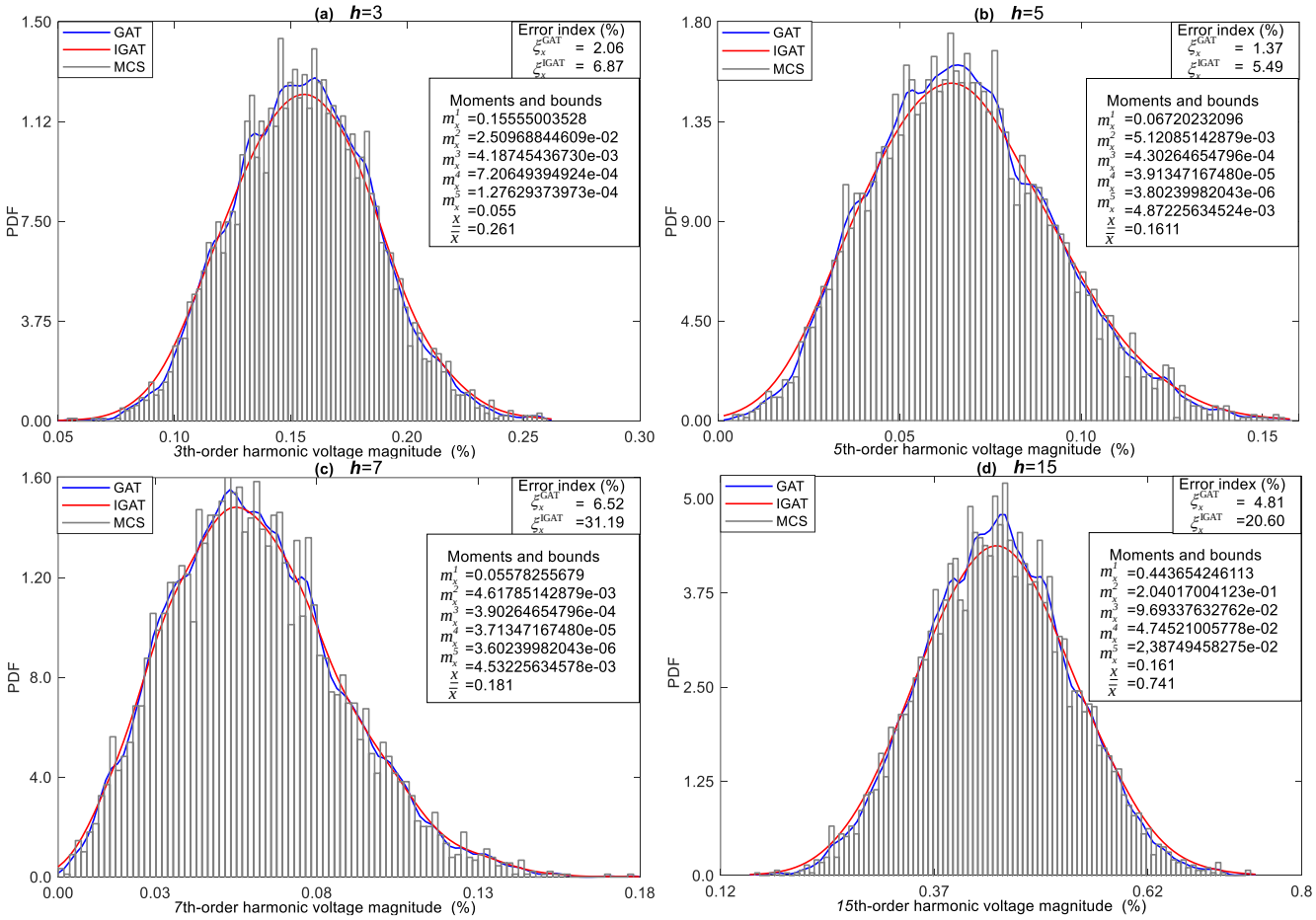

Fig. 7. *PDF curves of the* h*th-order harmonic voltage magnitude in phase a and node #30 with background harmonic interaction on a day of July at 12:00 p.m. (midday): (a) h= 3; (b) h=5; (c) h= 7; (c) h=15.*

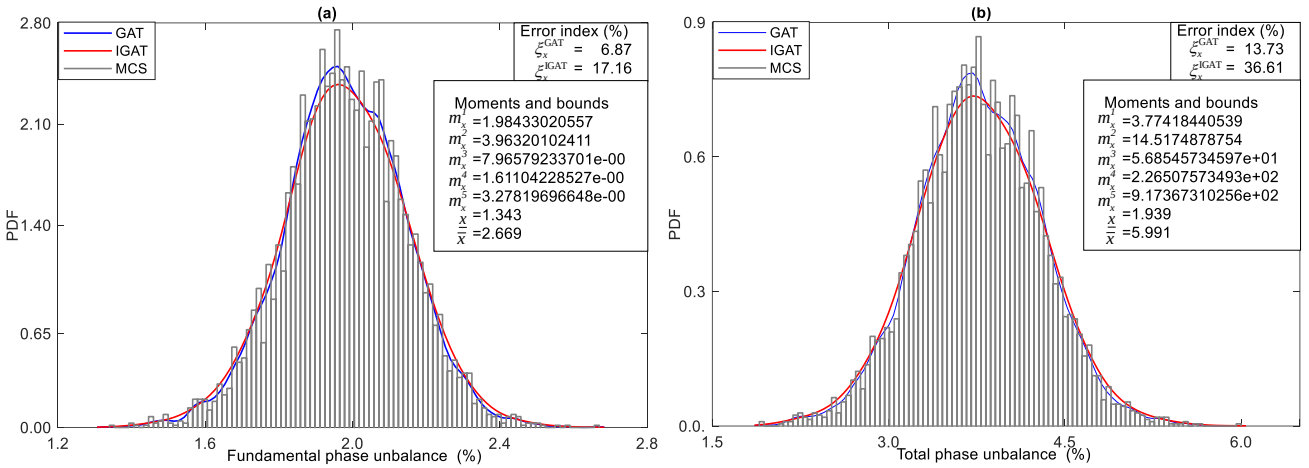

Fig. 8. *PDF curves of voltage unbalance in node #30 with background harmonic interaction on a day of July at 12:00 p.m. (midday): (a) fundamental phase unbalance; (b) total phase unbalance.*

7.1.5. Analysis of the impact of background harmonic interaction

In regard to node #30 in July, this section shows how the multiphase interaction of background harmonic voltage on PV harmonic current could strongly impact the resulting voltages for phases *a*, *b*, and *c*, see Fig. 9. Due to space limitations the results for other nodes are not shown. As can be observed in Fig. 9, the harmonic voltage amplitudes were different in each phase and were dependent on the loading and PV generation level. Thus, except for the 9th-order and 15th-order harmonics, the results show that these amplitudes in phase *c* were the highest and lowest in the phase *b*. The PV harmonic current value in phase *c* was higher than that of the other two phases, which was a consequence of a heavier PV generation allocation in phase *c* and a lighter allocation in phase *b*, i.e., 6 PV systems in phase *c* vs. 5 and 4 PV systems in phase *a* and *b*, respectively. The higher harmonic voltage values in phase *b*, for the 9th-order and 15th-order harmonics, could stem from the interaction between PV generation and load at the lowest PV harmonic current values that occurred at these harmonic orders. When the additional interaction was compared to the non-interaction condition, it was found that this similarly shifted the resulting PDFs of three phases. In fact, it increased values for every harmonic except for the 7th-order harmonic though the SRDN operated under unbalanced conditions. Conversely, the 7th-order harmonic showed an opposite trend and decreased its values. Moreover, the dispersion of PDFs remained almost unchanged and the phase with the highest and lowest harmonic voltage did not vary. This means that the interaction did not change voltage unbalance as indicated in Fig. 12. This provided sufficient justification to analyze in detail the multiphase interaction impact for harmonics focusing on a single phase (Fig. 10).

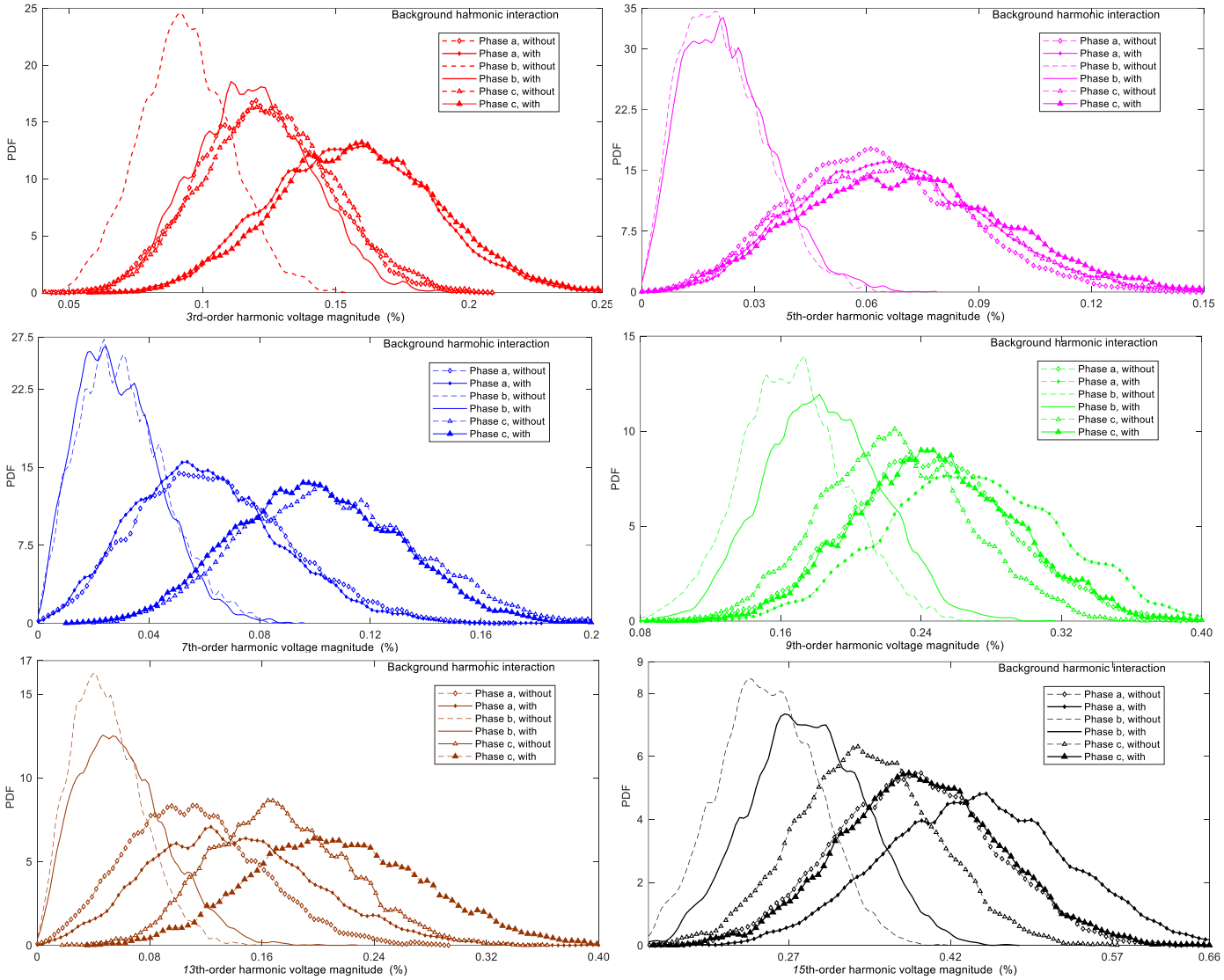

Fig. 9. *PDF curves of the 15th-order harmonic voltage magnitudes in node #30 and phases a, b, and c with/without background harmonic interaction on a day in July at 12:00 p.m. (midday).*

Fig. 10 summarizes the interaction impact for different harmonics at phase *a*. The month of July was selected to discuss this interaction impact since the PDF magnitudes had their highest levels. As a common behavior pattern, lower-order harmonic voltages (3rd-order, 5th-order, and 7th-order harmonics) tended to strongly modify most of the PV harmonic currents since significant shifts were found at high-order harmonic voltages despite their low PV harmonic currents (see Fig. 6). On the other hand, there was a great coupling between triplen harmonic voltages (3rd-order, 9th-order, and 15th-order harmonics) with larger increases. More specifically, the most significant harmonic voltage rise (27.2%) was in the 3rd-order harmonic, which had the highest PV current magnitude. This high interaction impact in triplen harmonics was due to the unbalanced conditions in the SRDN. However, the behavior of the lower-order harmonic voltages of positive and negative sequence (i.e., 5th-order and 7th-order harmonics) hardly varied (increase of about 3.5% for the 5th-order and -2.2% for the 7th-order).

The aggregated impact of background harmonic interaction on resulting harmonic voltages led to a moderate TPD_V rise of about 14.5% for January and 14.4% for July, (Fig. 11). However, as shown in Fig. 12, the impact on the voltage unbalance was very limited. For example in scenario #2, this low impact was mainly observed in TPU_V (Fig. 12b1) because of the change in the harmonic unbalance components (Fig. 12b2), where the TPU_{V^1} remained almost unchanged. Furthermore, the interaction did not contribute to a more ideal balanced case since the sequence of characteristic harmonics moved somewhat erratically away from this case. In other words, ratio $\Upsilon_V^{(2)h}$ changed to lower values for negative-sequence harmonics (5th-order and 11th-order harmonics) but also for positive- and zero-sequence harmonics (13th-order and 15th-order harmonics). As a result, variation in the TPU_V was minimal.

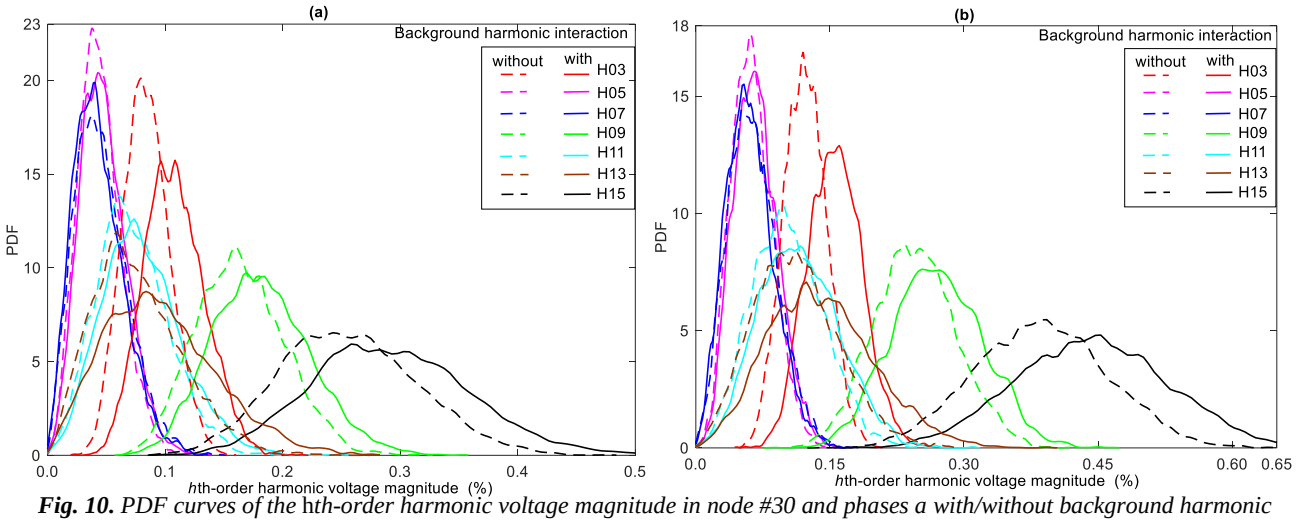

Fig. 10. *PDF curves of the* h*th-order harmonic voltage magnitude in node #30 and phases a with/without background harmonic interaction at 12:00 p.m. (midday) on a day in: (a) January(#1); (b) July(#2).*

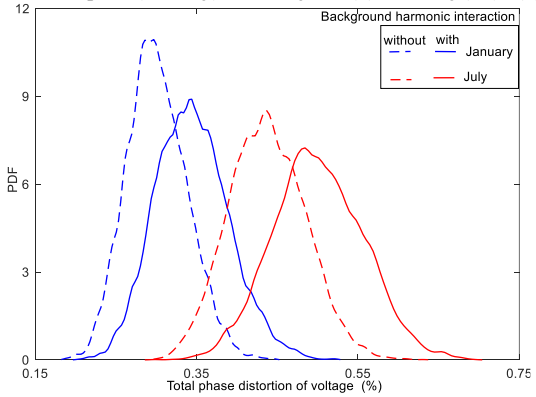

Fig. 11. *PDF curves of the total phase distortion of voltage in node #30 with/without background harmonic interaction on a day of January and July at 12:00 p.m. (midday)*

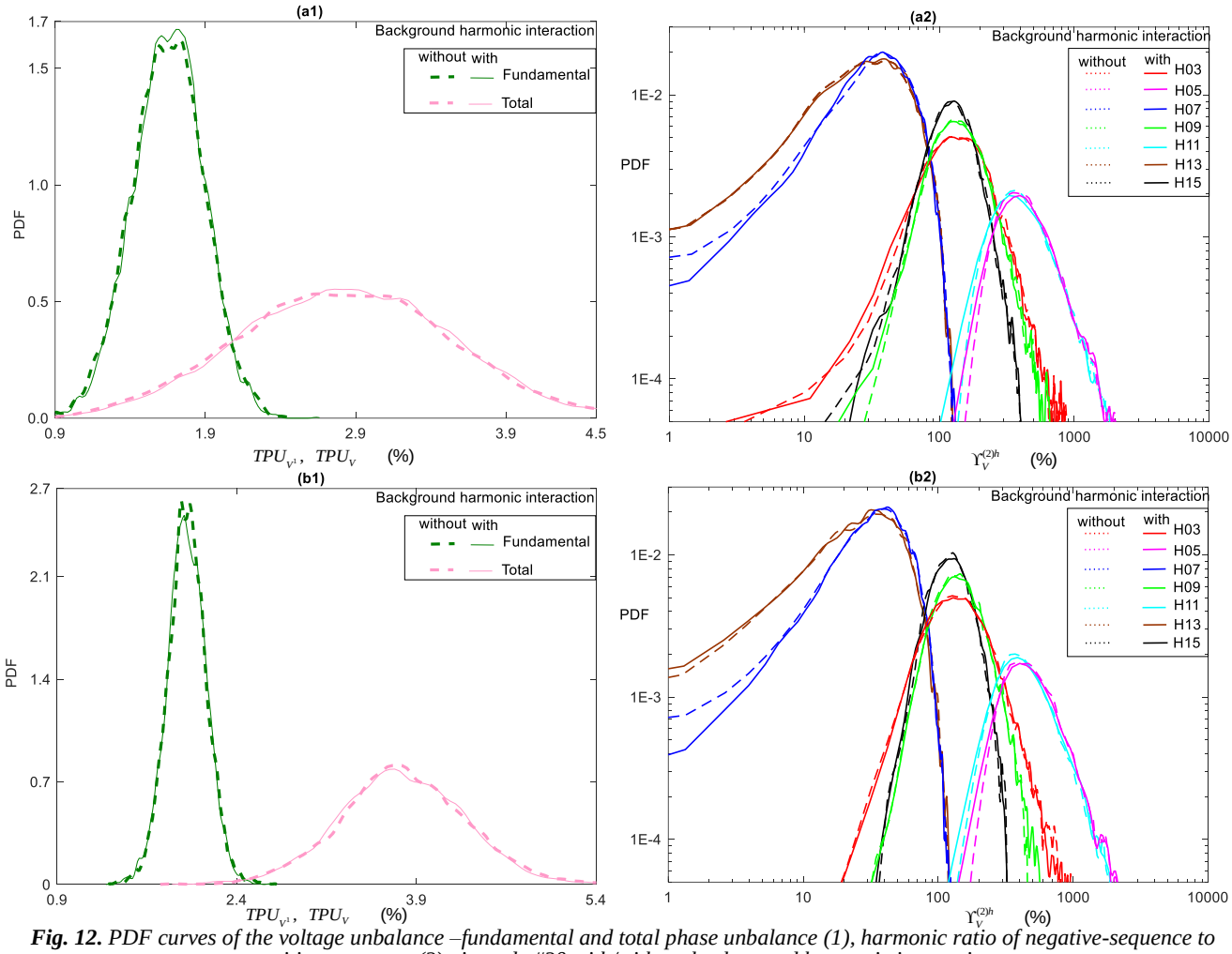

Fig. 12. *PDF curves of the voltage unbalance –fundamental and total phase unbalance (1), harmonic ratio of negative-sequence to positive-sequence (2)– in node #30 with/without background harmonic interaction at 12:00 p.m. (midday) on a day in: (a) January; (b) July.*

7.1.6. Meeting of regulatory limits

This section discusses the regulatory limit fulfilment for harmonic distortion and voltage unbalance in the SDRN. Fig. 13 presents the harmonic voltage profile for all SRDN nodes, focusing in phase *a*. The most harmonic orders met their harmonic voltage limit of compatibility level in the low voltage (LV) IEC standard [60]. However, the 15th-order harmonic voltages in some nodes in January were closer to the 0.4% level in [60]. In contrast, the harmonic voltages in July were even higher than in January. This was unacceptable for nodes #24 to #31. However, when the 0.5% limit in EN 50160 Std. [59] was assumed, this outcome was somewhat less important

Regarding the 15th-order harmonic voltages of the entire SRDN, their PDFs in each scenario were used to assess the violation probability of the compatibility level in [60]. A compatibility-level value is based on the 95% probability level, i.e., an α significance level below 5%. Therefore, a violation probability higher than a 5%-α level involves noncompliance with the regulatory limit. Based on the 0.4%-compatibility level in [60], Fig. 15a shows the violation probability for all of the SRDN nodes and phases, Nevertheless, the expected value in Fig. 13b for scenario #2 cannot be compared with the compatibility level. For example, the expected value at node #23 was 0.354%. (Fig. 13b) below the compatibility level. In contrast, Fig. 15a shows that the violation probability of harmonic voltage was 10.4%,higher than the 5%-significance level because of the dispersion. As a result, this node did not comply with the regulatory limit.

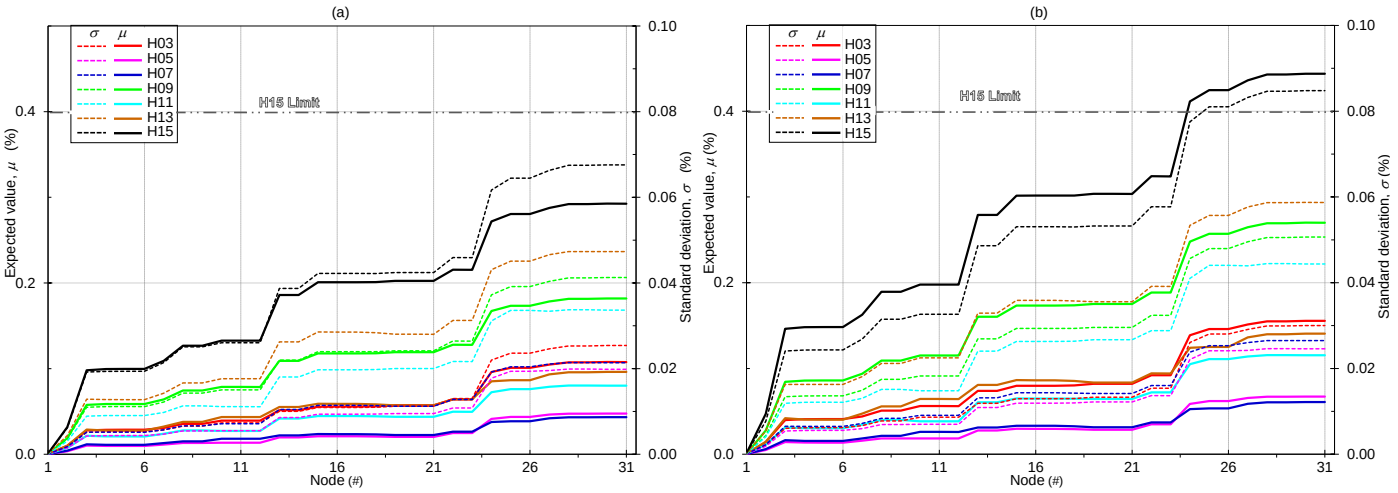

Fig. 13. *Expected value and standard deviation of* h*th-order harmonic voltage magnitude (phase a) with background harmonic interaction at 12:00 p.m. (midday) on a day in: (a) January; (b) July.*

Fig. 14 shows the voltage unbalance profile for all of the SRDN nodes in scenarios #1 and #2. In general, the voltage unbalance rose as the distance from the root node increased, though not always. It was assumed that the root node was a balanced three-phase source. Throughout the SRDN, the unbalanced location of PV and load currents caused unequal voltage drops, which produced unbalanced phase voltages. However, there was evidently a flatter distribution of the fundamental and total phase unbalance towards the root node than the distribution of the harmonic voltages in Fig. 13. The reason for this was that values of TPU_V were about 200-300% greater than the corresponding values of TPU_{V^1}. As a result, the harmonic unbalance components were very important but did not determine the shape of TPU_V, which followed the shape of TPU_{V^1}. As can be observed, there was no great change in TPU_{V^1} throughout the SRDN because the unbalanced PV fundamental-frequency currents were able to locally feed the closest unbalanced loads, and thus help to maintain a more balanced condition. In contrast, unbalanced PV harmonic currents flowed toward the root node and caused an increasing number of unequal harmonic voltage drops (Fig. 14).

Furthermore, Fig. 14 clearly shows that the sequence of characteristic harmonics was not as large as expected in the ideal balanced case. Even though the most important negative-sequence components were obviously the 5th-order and 11th-order harmonics, most harmonics tended to comprise both zero and negative-sequence components, as reflected in the negative-sequence in 3rd-order, 9th-order and 15th-order harmonics.

Regarding the regulatory limit for voltage unbalance of all of the SRDN nodes, their PDFs allowed the violation probability assessment of the 2%-compatibility level limit in [59,60] (see Fig. 15b). Despite the fact that Fig. 14b shows the expected value of total phase unbalance, at each SRDN node, this value cannot be compared with the compatibility level. For example, as shown in Fig. 14b, the expected value at node #10 in scenario #2 was 1.99%, which was below the compatibility level. Nevertheless, as highlighted in Fig. 15b, the violation probability of the total phase unbalance was 60.99%, which was higher than the 5%-significance level because of dispersion. Accordingly, this node did not fulfil the regulatory limit.

The results were worse when the regulatory limit fulfilment for harmonic distortion (Fig. 15a) and voltage unbalance (Fig. 15b) were compared. This higher level of noncompliance was not only due to unbalanced PV currents but also to PV harmonic distortion, which significantly increased total versus fundamental phase unbalance.

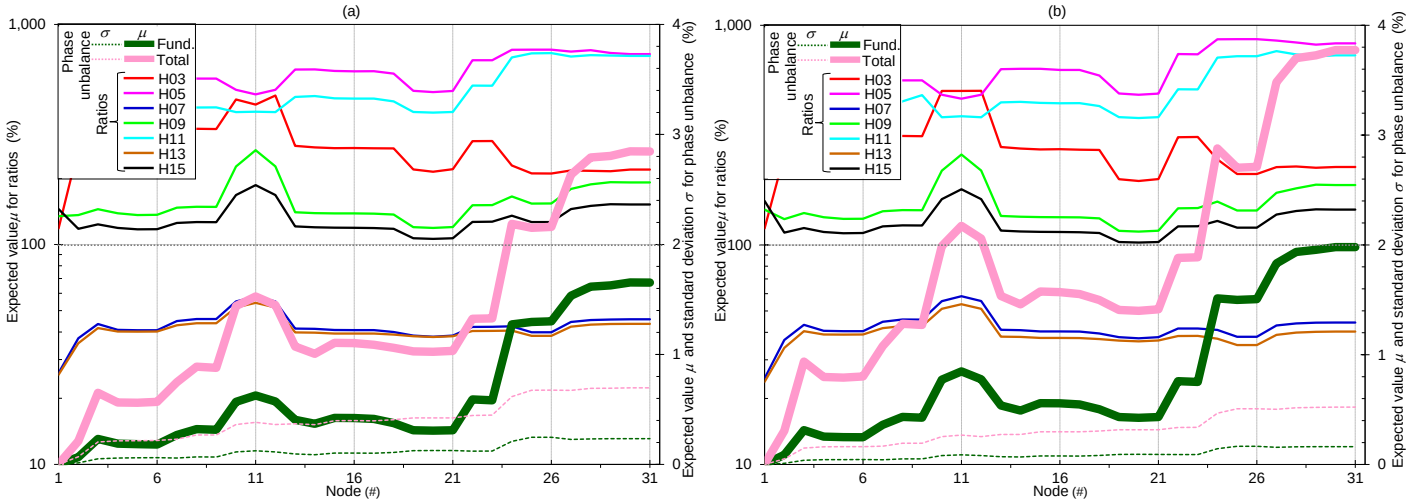

Fig. 14. *Expected value and standard deviation of voltage unbalance (fundamental and total phase unbalance, harmonic ratio of the negative-sequence to the positive-sequence) with background harmonic interaction at 12:00 p.m. (midday) on a day in: (a) January; (b) July.*

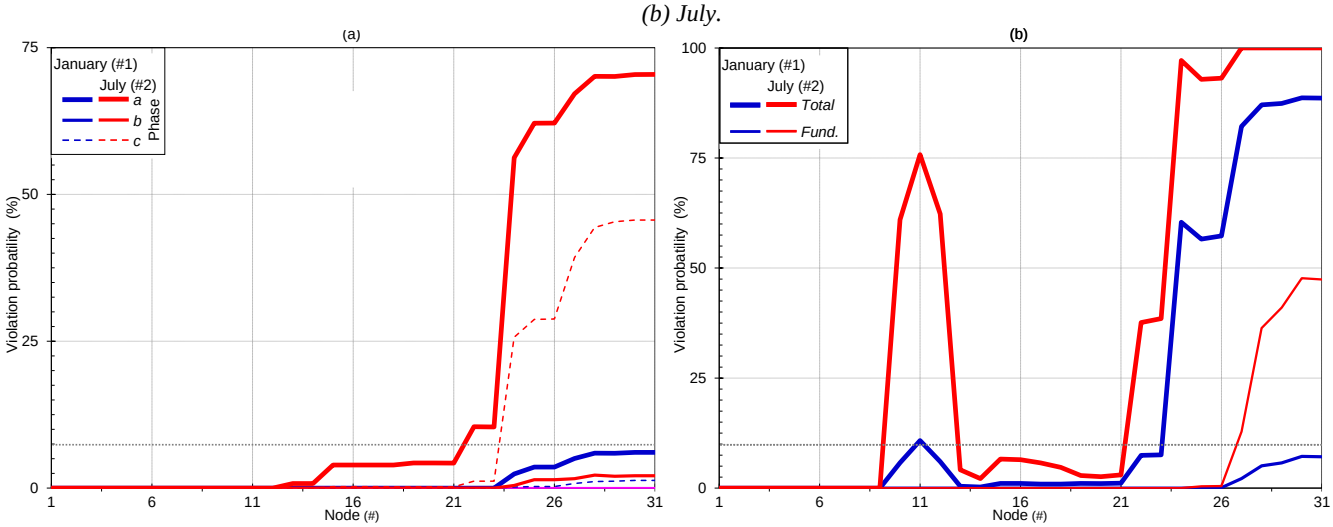

Fig. 15. *Violation probability, based on regulations, for the whole nodes during a day in January/July at 12:00 p.m. (midday) for: (a) 15h-order harmonic voltage; (b) fundamental and total phase unbalance of voltage.*

8. Conclusions

This study developed a GAT for solving iterative multiphase HLFs in SRDNs with input uncertainties from PV systems. This GAT was able to successfully deal with unbalanced conditions. Particular attention was given to the procedure to obtain the set of descriptive measurements used to stochastically characterize the output variables (harmonic distortion and voltage unbalance). Various improvements were also implemented to reduce the computational efforts to obtain these measurements. For this purpose, an innovative combination of the PEM and complex AA was adopted. Another important feature of the GAT was the use of the LGSA to achieve the best reconstruction for the output variables, bounded on a finite interval. The GAT incorporated the IHP method into the multiphase framework, which made it possible to also handle background harmonic interaction. Moreover, the GAT was able to take into account the double uncertainty in the PV harmonic injection (magnitude and phase angle), which is more realistic in the operation of SRDNs.

The results obtained for a real SRDN demonstrated that the GAT was well suited for the assessment of uncertainty propagation in iterative HLFs, and that it could be effectively applied to SRDNs in unbalanced conditions. The comparison of these results with those obtained with MCS showed that the GAT has a satisfactory level of accuracy with a shorter computational time. Although the calculation speed of the GAT was slightly less than that of IGAT, it was found to be more accurate.

The numerical results indicated that the impact of background harmonic interaction cannot be neglected. Thus, the aggregated impact of background harmonic interaction on the resulting harmonic voltages led to a moderate increase in TPD_V . However, as expected, this interaction did not have a significant impact on voltage unbalance.

Regarding regulatory limit fulfilment, a high level of noncompliance was found to occur in July, due to voltage unbalance limits. The reason for this was not only the unbalanced PV currents but also mainly PV harmonic distortion. Since the probability of noncompliance was particularly high, equipment damage was to be expected. This research and the numerical results of its case study highlight the usefulness of the GAT for the application of harmonic standards.

9. References

[1] Dubey A, Chandekar A, Bopche M, Nimkar P, Bangde P. A Preliminary study on harmonics generated by the grid-connected PV system on distribution. Proceedings of the 2018 International Conference on Smart Electric Drives and Power System; Nagpur, India; 2018. p. 50-3

[2] Aourir M, Abouloifa A, Lachkar I, Aouadi C, Giric F, Guerrero JM. Nonlinear control and stability analysis of single stage grid-connected photovoltaic systems. Int J Elec Power Energy Syst 2020;115:Article 105439.

[3] Camilo FM, Pires VF, Castro R, Almeida ME. The impact of harmonics compensation ancillary services of photovoltaic microgeneration in low voltage distribution networks. Sust Cities Soc 2018;39:449–58.

[4] Phannil N, Jettanasen C, Ngaopitakkul A. Power quality analysis of grid connected solar power inverter. Proceedings of the 3rd IEEE International Future Energy Electronics Conference and ECCE Asia; Kaohsiung, Taiwan; 2017. p. 1508-13.

[5] Caamaño-Martín E, Laukamp H, Jantsch M, Erge T, Thornycroft J, De Moor H, et al. Interaction between photovoltaic distributed generation and electricity networks. Prog Photovoltaics Res Appl 2008;16:629–43.

[6] Macedo WN, Zilles R. Influence of the power contribution of a grid-connected photovoltaic system and its operational particularities. Energy Sustain Dev 2009;13(3):202–11.

[7] Hernández JC, Ortega MJ, De la Cruz J, Vera D. Guidelines for the technical assessment of harmonic, flicker and unbalance emission limits for PV-distributed generation. Electr Pow Syst Res 2011;81(7):1247–57.

[8] Menti A, Zacharias T, Milias-Argitis J. Harmonic distortion assessment for a single-phase grid-connected photovoltaic system. Renew Energ 2011;36:360–8.

[9] Ortega MJ, Hernandez JC, García OG. Measurement and assessment of power quality characteristics for photovoltaic systems: Harmonics, flicker, unbalance, and slow voltage variations. Electr Pow Syst Res 2013;96:23–35

[10] Domagk M, Meyer J, Hoven M, Malekian K, Safargholi F, Kuech K. Probabilistic comparison of methods for calculating harmonic current emission limits. Proceedings of the 2017 IEEE PowerTech; Manchester, UK; 2017; p. 1-6.

[11] Špelko A, Blažič B, Papič I, Pourarab M, Meyer J, Xu X, Djokic SZ. CIGRE/CIRED JWG C4.42: Overview of common methods for assessment of harmonic contribution from customer installation. Proceedings of the 2017 IEEE PowerTech; Manchester, UK; 2017; p. 1-6.

[12] Bollen M, Schwaegerl C, Schmitt S. Distributed energy resources and waveform distortion. Proceedings of the 19th International Conference on Electricity Distribution; Vienna, Austria; 2007; p. 1-4.

[13] Hernandez JC, De La Cruz J, Vidal PG, Ogayar B. Conflicts in the distribution network protection in the presence of large photovoltaic plants: the case of ENDESA. Int Trans Electr Energ Syst 2013;23(5):669–88.

[14] Rogalla S, Ackermann F, Bihler N, Moghadam H, Stalter O. Source-driven and resonance-driven harmonic interaction between PV inverters and the grid. Proceedings of the IEEE 43rd Photovoltaic Specialists Conference; Portland, OR, USA; 2016. p. 1399-1404.

[15] Schwanz D, Möller F, Rönnberg SK, Meyer J, Bollen MHJ. Stochastic assessment of voltage unbalance due to single-phase-connected solar power. Proceedings of the 17th International Conference on Harmonics and Quality of Power; ICHQP; Belo Horizonte, Brazil; 2016; p. 1-9.

[16] Schwanz D, Möller F, Rönnberg SK, Meyer J, Bollen MHJ. Stochastic assessment of voltage unbalance due to single-phase-connected solar power. IEEE Trans Power Delivery 2017;32(2): 852–861.

[17] Bracale A, Carpinelli G, Caramia P, Russo A, Varilone P. Point estimate schemes for probabilistic load flow analysis of unbalanced electrical distribution systems with wind farms. Proceedings of the 14th International Conference on Harmonics and Quality of Power; ICHQP 2010; Bergamo, Italy; 2010. p.1-6.

[18] Silva MM, Losada y Gonzalez M, Uturbey W, Carrano EG, Silva SR. Evaluating harmonic voltage distortion in load-variating unbalanced networks using Monte Carlo simulations. IET Gener Transm Distrib 2015;9(9):855–65.

[19] Wang S, Liu X, Wang K, Wu L, Zhang Y. Tracing harmonic contributions of multiple distributed generations in distribution systems with uncertainty. Int J Elec Power Energy Syst 2018;95:585–91.
[20] Galvani S, Marjani SR, Morsali J, Jirdehi MA. A new approach for probabilistic harmonic load flow in distribution systems based on data clustering. Electr Pow Syst Res 2019;176:Article 105977.
[21] Xu W, Martin JR, Dommel HW. A multiphase harmonic load flow solution technique. IEEE Trans Power Syst 1991;6(1):174–82.
[22] Valcarcer M, Mayordomo JG. Harmonic power flow for unbalanced systems. IEEE Trans Power Delivery 1993;8:2052–59.
[23] Herraiz S, Sainz L, Clua J. Review of harmonic load flow formulations. IEEE Trans Power Deliv 2003;18:1079–87
[24] Bosovic A, Renner H, Abart A, Traxler E, Meyer J, Domagk M, Music M. Validation of aggregated harmonic current source models based on different customer type configurations. Proceedings of the 2016 Electric Power Quality and Supply Reliability; Tallinn, Estonia; 2016; p. 1-8.
[25] Bosovic A, Renner H, Abart A, Traxler E, Meyer J, Domagk M, Music M. Deterministic aggregated harmonic source models for harmonic analysis of large medium voltage distribution networks. IET Gener Transm Distrib 2019;13(19):4421–4430.
[26] Romero AA, Zini HC, Ratta G, Dib R. Harmonic load-flow approach based on the possibility theory. IET Gener Transm Distrib 2011;5(4):393–404.
[27] M. Lehtonen. A method probabilistic harmonic load-flow analysis in power systems. Eur Trans Electr Power 1998;1:47–50.
[28] Mohammadi M. Probabilistic harmonic load flow using fast point estimate method. IET Gener Transm Distrib 2015;9(13):1790–9.
[29] Yu G, Lin T. 2m+1 point estimate method for probabilistic harmonic power flow. Proceedings of the 2016 IEEE Power and Energy Society General Meeting; Boston, MA, USA; 2016. p.1-5.
[30] Nasrfard-Jahromi F, Mohammadi M. Probabilistic harmonic load flow using an improved kernel density estimator. Int J Elec Power Energy Syst 2016;78:292–8.
[31] Kiani-Moghaddam M, Shivaie M, Weinsier PD. A techno-economic multi-objective model for hybrid harmonic filter planning considering uncertainty in non-linear loads. Int J Elec Power Energy Syst 2019;112:339–52.
[32] Xia D, Heydt GT. Harmonic power flow studies - Part II Implementation and practical application. IEEE Trans Power Appar Syst 1982;PAS-101(6):1266–70.
[33] Sharma V, Fleming RJ, Niekamp L, An iterative approach for analysis of harmonic penetration in pow transmission networks. IEEE Trans Power Delivery 1991;6(4):1698–1706.
[34] Caramia P, Carpinelli G, Rossi F, Verde P. Probabilistic iterative harmonic analysis of power systems. IEE Gener Transm Distrib 1994;141(4):32–38.
[35] Carpinelli G, Esposito T, Varilone P, Verde P. First-order probabilistic harmonic power flow. IEE Gener Transm Distrib 2001;148(6):541–48.
[36] Esposito T, Carpinelli G, Varilone P, Verde P. Probabilistic harmonic power flow for percentile evaluation. Proceedings of the 2001 Canadian Conference on Electrical and Computer Engineering; Toronto, Ontario, Canada; 2001. p.831-8.
[37] Bonner A, Grebe T, Gunther E, Hopkins L, Marz MB, et al. Modeling and simulation of the propagation of harmonics in Electric power networks. Part II: Sample systems and examples. IEEE Trans Power Delivery 1996;11(1):466–74.
[38] Ruiz-Rodriguez FJ, Hernandez JC, Jurado F. Probabilistic load flow for radial distribution networks with photovoltaic generators. IET Renew Power Gen 2012;6(2):110–21.
[39] Ruiz-Rodriguez FJ, Hernandez JC, Jurado F. Probabilistic load flow for photovoltaic distributed generation using the Cornish-Fisher expansion. Electr Pow Syst Res 2012;89:129–38.
[40] Ruiz-Rodriguez FJ, Hernandez JC. Jurado F. Voltage unbalance assessment in secondary radial distribution networks with single-phase photovoltaic systems. Int J Elec Power Energy Syst 2015;64:646–654.
[41] Silva D. Probabilistic load flow considering dependence between input nodal powers. IEEE Trans Power Appar Syst 1984:1524–30.
[42] Zhang G, Xu W. Estimating harmonic distortion levels for systems with random-varying distributed harmonic-producing loads. IET Gener Transm Distrib 2008;2:847–55.
[43] Swief RA, Salam TSA. PV impact on distribution system performance following the grey wolf algorithm. Proceedings of the Nineteenth International Middle East Power Systems Conference; MEPCON; Cairo, Egypt; 2017; p. 437-444.
[44] Bayer B, Matschoss P, Thomas H, Marian A. German experience with integrating PV systems into the low-voltage grids. Renew Energy 2018;119:129–141.
[45] Freitas S, Santos T, Brito MC. Impact of large scale PV deployment in the sizing of urban distribution transformers. Renew Energy 2018;119:767–776.
[46] Aien M, Fotuhi-Firuzabad M, Aminifar F. Probabilistic load flow in correlated uncertain environment using unscented transformation. IEEE Trans Power Syst 2012;27:2233–41.

[47] Kabir MN, Mishra Y, Bansal RC. Probabilistic load flow for distribution systems with uncertain PV generation. Appl Energ 2016;163:343–351.
[48] Li Q, Wang X, Rong S. Probabilistic load flow method based on modified Latin hypercube-important sampling. Energies 2018;11: 3171.
[49] Sossan F, Nespoli L, Medici V, Paolone M. Unsupervised disaggregation of Photovoltaic production from composite power flow measurements of heterogeneous prosumers. IEEE Trans Ind Inf 2018;14(9): 3904–3913.
[50] Hernandez JC, Ruiz-Rodriguez FJ, Jurado F. Technical impact of photovoltaic-distributed generation on radial distribution systems: Stochastic simulations for a feeder in Spain. Int J Electr Pow Energ Syst 2013;50:25–32.
[51] Fan M, Vittal V. Probabilistic Power flow studies for transmission systems with photovoltaic generation using cumulants. IEEE Trans Power Syst 2012;27:2251–2261.
[52] Hernandez JC, Ruiz-Rodriguez FJ, Jurado F. Modelling and assessment of the combined technical impact of electric vehicles and photovoltaic generation in radial distribution systems. Energy 2017; 141:316–332.
[53] Ruiz-Rodriguez FJ, Hernandez JC, Jurado F. Voltage behaviour in radial distribution systems under the uncertainties of photovoltaic systems and electric vehicle charging loads. Int Trans Electr Energ Syst 2018;28:e2490.
[54] Dopazo JF, Klitin OA, Sasson MA. Stochastic load flows. IEEE Trans Power Appl Syst 1975;94:752–759.
[55] Xue F, Xie W, Xie P, Pan Z, Ren J, Nie Y, et al. Unbalanced three-phase distribution system power flow with distributed generation using affine arithmetic. Proceedings of the 5th International Conference on Electric Utility Deregulation and Restructuring and Power Technologies; Changsha, China; 2015. p. 822-9.
[56] Wu C, Wen F, Lou Y, Xin F. Probabilistic load flow analysis of photovoltaic generation system with plug-in electric vehicles. Int J Electr Pow Energ Syst 2015;64:1221-1228.
[57] Wang S, Wang C, Liu R. Fuzzy interval algorithm based computation of power flow in distribution network. Autom Electr Power Syst 2000;24(20):19–22.
[58] Billinton R, Allan R. Reliability evaluation of power systems. 2nd ed., New York: Plenum Press; 1996.
[59] EN 50160. Voltage characteristics of electricity supplied by public distribution systems; 2000.
[60] IEC 61000-2-2+AMD1+AMD2. Electromagnetic compatibility - Environment - Compatibility levels for low-frequency conducted disturbances and signalling in public low-voltage power supply systems; 2002, 2017, 2018.
[61] Caramia P, Carpinelli G, Esposito T, Varilone P. Evaluation methods and accuracy in probabilistic harmonic power flow. Eur Trans Electr Power 2003;13:391–8.
[62] Rosenblueth E. Point estimates for probability moments. Proc Nat Acad Sci 1975;72:3812–4.
[63] Manson G. Calculating frequency response functions for uncertain systems using complex affine analysis. J Sound Vib 2005;288:487–521.
[64] Tovilović DM, Rajaković NLJ. The simultaneous impact of photovoltaic systems and plug-in electric vehicles on the daily load and voltage profiles and the harmonic voltage distortions in urban distribution systems. Renew Energ 2015;76:454–64.
[65] Sakar S, Balci ME, Abdel Aleem SHE, Zobaa AF. Increasing PV hosting capacity in distorted distribution systems using passive harmonic filtering. Electr Pow Syst Res 2017;148:74–86.
[66] Peterson B, Rens J, Botha G, Meyer J, Desmet J. Evaluation of harmonic distortion from multiple renewable sources at a distribution substation. Proceedings of the 2017 IEEE International Workshop on Applied Measurements for Power Systems; AMPS; Liverpool, UK; 2017; p. 1-6.
[67] Torquato R, Shi Q, Xu W, Freitas W. A Monte Carlo simulation platform for studying low voltage residential networks. IEEE Trans Smart Grid 2014;5(6):276–76.
[68] Bin C, Ruoying Y, Dongsheng D, Xiangyan W. Probabilistic harmonic analysis on distributed photovoltaic integration considering typical weather scenarios. Proceedings of the 2nd Asia Conference on Power and Electrical Engineering; ACPEE 2017; Shanghai, China; 2017. p.1-8.
[69] Jannesar MR, Sedighi A, Savaghebi M, Anvari-Moghaddam A, Guerrero JM. Optimal probabilistic planning of passive harmonic filters in distribution networks with high penetration of photovoltaic generation. Int J Elec Power Energy Syst 2019;110:332–48.
[70] Hong HP. An efficient point estimate method for probabilistic analysis. Reliab Eng Syst Saf 1998;59:261–7.
[71] de Figueiredo LH, Stolfi J. Affine arithmetic: Concepts and applications. Numer Alg 2004;37(1–4):147–58.
[72] Ruiz-Rodriguez FJ, Hernandez JC, Jurado F. Harmonic modelling of PV systems for probabilistic harmonic load flow studies. Int J Circ Theor Appl 2015;43:1541–65.
[73] IEC 61000-4-7. Electromagnetic compatibility - Part 4-7: Testing and measurement techniques - General guide on harmonics and interharmonics measurements and instrumentation, for power supply systems and equipment connected thereto; 2008.
[74] IEEE 1159. IEEE Recommended practice for monitoring electric power quality; 1995.

[75] Fortescue CL. Method of symmetrical coordinates applied to the solution of polyphase networks. Trans AIEE 1918;37(II):1027–140.
[76] Chicco G, Postolache P, Toader C. Analysis of three-phase systems with neutral under distorted and unbalanced conditions in the symmetrical component-based framework. IEEE Trans Power Delivery 2007;22(1):674–83.
[77] Comba JLD Stolfi J. Affine arithmetic and its applications to computer graphics. Proceedings of the Brazilian Symp. Computer Graphics and Image Processing; Brazil; 1993. p. 9-18.
[78] IEEE Power Engineering Society Task Force on Harmonics Modeling and Simulation. Tutorial on harmonics modeling and simulation. IEEE Power Engineering Society; 1998.
[79] Arrillaga J, Smith BC, Watson N, Wood A. Power system harmonic analysis. Chichester: John Wiley & Sons, Ltd.; 2003.
[80] Bonner A, Grebe T, Gunther E, Hopkins L, et al. Modeling and simulation of the propagation of harmonics in Electric power networks. Part II: Concepts, models, and simulation techniques. IEEE Trans Power Delivery 1996;11(1):452–65.
[81] McCullagh P. Tensor methods in statistics. London: Chapman and Hall; 1987.
[82] Cornish EA, Fisher RA. Moments and cumulants in the specification of distributions. Revue de l'Institut International de Statis 1937;4:307–20.
[83] Cramer H. Mathematical methods of statistics. Princeton Un.: Princeton, NJ; 1946.
[84] Blanco AM, Grevener A, Müller S, Meyer J, Schegner P. Stochastic harmonic load model of residential users based on measurements Proceedings of the 2015 IEEE PowerTech; Eindhoven, Netherlands; 2015; p. 1-6.
[85] Hernandez JC, Ortega MJ, Medina A. Statistical characterisation of harmonic current emission for large photovoltaic plants. Int Trans Electr Energ Syst 2014;24:1134–50..
[86] Kendall MG, Stuart A. The advanced theory of statistics. Vol. I. London: Charles Grin and Company Limited; 1963.
[87] Papoulis A, Pillai S. Probability, random variables, and stochastic processes. 4th ed. New York: McGraw-Hill; 2002.
[88] Xia D, Heydt GT. Harmonic power flow studies: Part I - Formulation and solution, Part II - Implementation and practical application. IEEE Trans Power Apparat Syst 1982;101:1257–70.
[89] Parihar SS, Malik N. Power flow analysis of balanced radial distribution system with composite load model. Proceedings of the 2nd Conference on Recent Developments in Control, Automation & Power Engineering; Noida, India; 2017. p. 160–5.
[90] Kersting WH. Distribution system modeling and analysis. 3rd ed. New Mexico: CRC Press; 2002.
[91] Wang S, Han L, Wu L. Uncertainty tracing of distributed generations via complex affine arithmetic based unbalanced three-phase power flow. IEEE Trans Power Syst 2015;30(6):3053–62.
[92] Chen P, Tao S, Xiao X. Uncertainty level of voltage in distribution network: an interval model and application in centralised storage location. IET Gener Transm Distrib 2017;11(14):3628–36.
[93] Jorgensen P. A new method for performing probabilistic production simulations by means of moments and Legendre series. IEEE Trans Power Syst 1991;6(2):567–75.